Land-based Infrared Imagery for Marine Mammal Detection

Joseph Graber

A thesis

submitted in partial fulfillment of the

requirements for the degree of

Master of Science in Mechanical Engineering

University of Washington

2011

Program Authorized to Offer Degree:

Department of Mechanical Engineering

University of Washington
Graduate School

This is to certify that I have examined this copy of a master’s thesis by

Joseph Graber

and have found that it is complete and satisfactory in all respects,
and that any and all revisions required by the final
examining committee have been made.

Committee Members:

____
Brian Polagye

____
Jim Thomson

____
Andy Jessup

Date: ______________________________

Signature ________________________

Date ___________________________

University of Washington

Abstract

Land-based Infrared Imagery for Marine Mammal Detection

Joseph Graber

Chair of the Supervisory Committee:
Research Assistant Professor Brian Polagye
Mechanical Engineering

A land-based infrared (IR) camera is used to detect endangered Southern Resident killer whales in Puget Sound, Washington, USA. The observations are motivated by a proposed tidal energy pilot project, which will be required to monitor for environmental effects. Potential monitoring methods also include visual observation, passive acoustics, and active acoustics. The effectiveness of observations in the infrared spectrum is compared to observations in the visible spectrum to assess the viability of infrared imagery for cetacean detection and classification.

Imagery was obtained at Lime Kiln Park, Washington from 7/6/10-7/9/10 using a FLIR Thermovision A40M infrared camera (7.5-14μm, 37°HFOV, 320x240 pixels) under ideal atmospheric conditions (clear skies, calm seas, and wind speed 0-4 m/s). Whales were detected during both day (9 detections) and night (75 detections) at distances ranging from 42 to 162 m. The temperature contrast between dorsal fins and the sea surface ranged from 0.5 to 4.6 °C. Differences in emissivity from sea surface to dorsal fin are shown to aid detection at high incidence angles (near grazing). A comparison to theory is presented, and observed deviations from theory are investigated. A guide for infrared camera selection based on site geometry and desired target size is presented, with specific considerations regarding marine mammal detection. Atmospheric conditions required to use visible and infrared cameras for marine mammal detection are established and compared with 2008 meteorological data for the proposed tidal energy site. Using conservative assumptions, infrared observations are predicted to provide a 74% increase in hours of possible detection compared with visual observations.

TABLE OF CONTENTS

LIST OF FIGURES

LIST OF TABLES

ACKNOWLEDGMENTS

I wish to thank my committee members, Dr. Brian Polagye, Dr. Jim Thomson, and Dr. Andy Jessup for their time, ideas, and support. Without their help this project would not have been possible. Ruth Branch, thank you for sharing your knowledge of infrared optics and for your thoughtful feedback. I would like to thank the University of Washington's Applied Physics Laboratory for supplying the infrared camera used for the field observations of this study. The funding for this project was provided by the Department of Energy (DOE) and Snohomish County Public Utility District and for that I am grateful. Thanks to Dr. Jason Wood and The Whale Museum for hosting us at Lime Kiln Park and sharing their extensive knowledge of Southern Resident killer whales. Thank you to Dr. Scott Veirs of Beam Reach Marine Science and Sustainability School for his communications throughout the project and providing hydrophone recordings of marine mammal vocalizations. Finally, I would like to express my deepest gratitude to my wife, Sejal Graber, for her unyielding support of all my endeavors and for reminding me to take breaks and eat throughout this project.

Chapter 1 - Introduction

The detection and monitoring of marine mammals is required for a wide range of disciplines from ecological impact assessments to behavioral and biological studies. Current methods include passive acoustic monitoring, active acoustic monitoring, visual observation, and visual imagery (digital video and still cameras). Each method is faced with challenges. Passive acoustic monitoring relies on mammal vocalizations or echolocations, which are imperfect indicators of species presence or behavior (Greene & Chase, 1987). In addition, the local ambient noise must be low enough to allow for the sounds from marine mammals to be distinguished from the background. Active acoustic monitoring introduces anthropomorphic noise into the marine environment and has the potential to affect cetacean behavior (Schoonmaker, Dirbas, Podobna, Wells, Boucher, & Oakley, 2008). Visual observation is widely used, but is limited by atmospheric conditions, including ambient light, visibility, and sea state. Infrared (IR) imagery has the potential to improve upon visual observations by enabling nighttime detections. However, like observations in the visible spectrum, IR imagery is only effective under a subset of atmospheric conditions and sea states and can only detect marine mammals on the surface. The primary purpose of this study is to evaluate the efficacy of using infrared imaging for site characterization and marine mammal monitoring of a proposed tidal energy project in Puget Sound.

1.1 Tidal Energy in Puget Sound

In 2006 Washington state voters passed initiative I-937, requiring electric utilities to generate 15% of their power from renewable resources by 2020. Conventional hydroelectric power, accounting for 64% of Washington's current energy supply, is specifically excluded from the definition of renewable (US Energy Information Administration, 2010). To meet this obligation, Snohomish County Public Utility District (PUD) is investigating adding tidal energy to its renewable resource portfolio. They are currently planning a pilot project for deployment in northern Admiralty Inlet, Puget Sound in early 2013.

Tidal energy is the extraction of energy from tidal currents which are driven by the gravitational interaction between the sun, moon, and the earth's oceans. At northern and southern latitudes, the earth's oceans rise and fall twice daily (semi-diurnal tide). When the ocean level raises, water floods into estuaries, and when it falls, water ebbs back out. Hydrokinetic turbines placed in areas of high tidal flow (such as estuary inlets) extract energy from the moving water in the same way that wind turbines extract energy from moving air. As water flows over the blades of a hydrokinetic turbine a lifting force is generated that turns an electric generator. Snohomish County PUD proposes to deploy two 10 meter diameter tidal turbines designed by Open Hydro. Figure 1.1 shows a 3-D model of the chosen turbine which will be deployed on the sea floor (approximately 60 meters deep) using a gravity base foundation. The turbine blades are symmetric and rotate in both directions allowing energy to be generated from both flood and ebb currents.

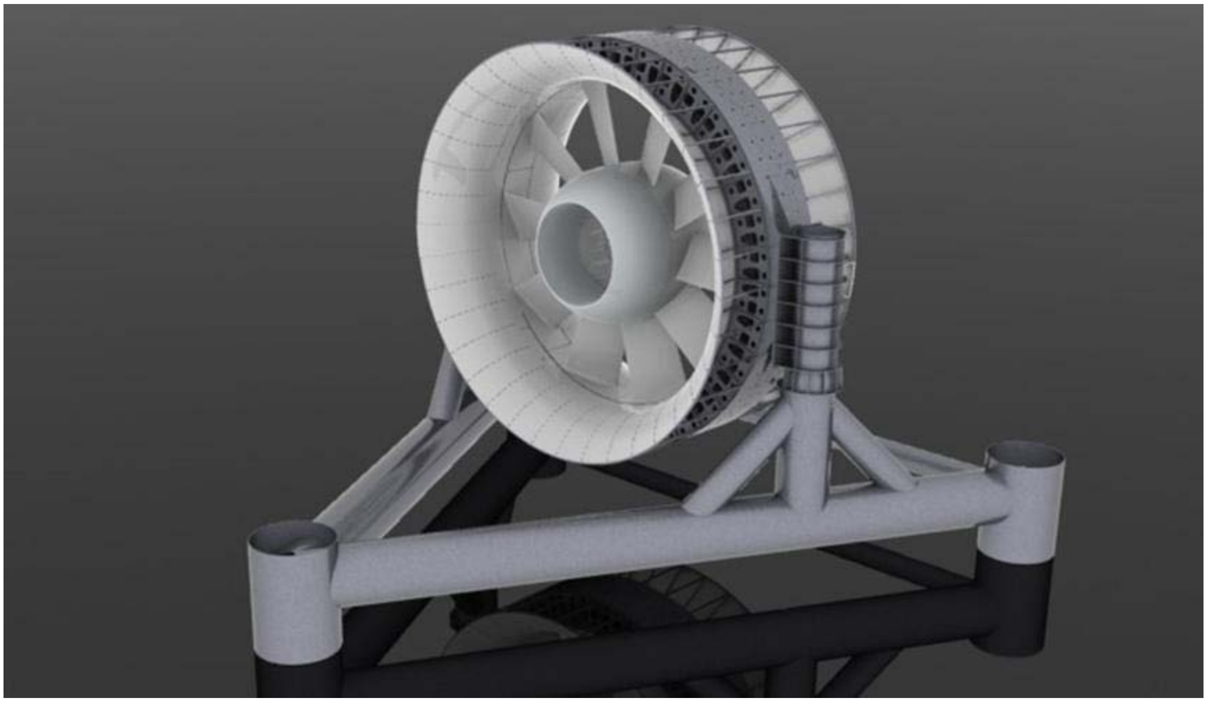

Figure 1.1 3-D model of the Open Hydro tidal energy turbine selected by the Snohomish County PUD for their pilot project in Admiralty Inlet.

1.1.1 Site Description

Admiralty Inlet is 5 km wide and serves as the primary inlet to Puget Sound. Tidal currents can exceed 3 m/s, making it a prime location for tidal energy development. As show in Figure 1.2, the location of the proposed pilot project is on the east side of Admiralty Inlet about 1 km southwest of Fort Casey State Park. The Admiralty Head lighthouse at Fort Casey State Park offers the best vantage point for observation of the proposed turbine site.

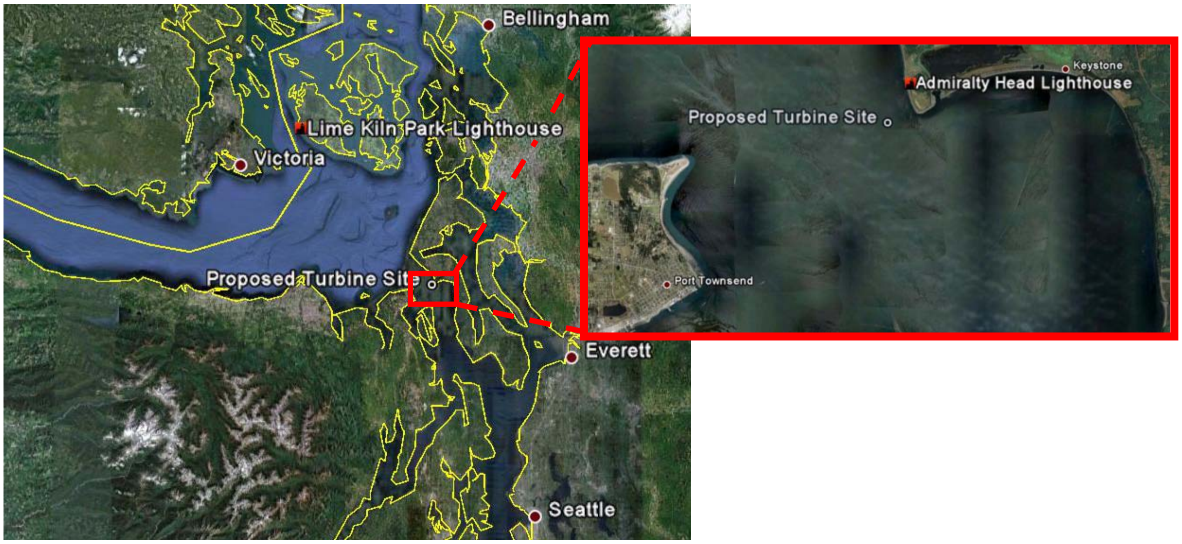

Figure 1.2 Location of the proposed Snohomish County PUD tidal energy project.

Admiralty Inlet is a known transit point for endangered Southern Resident killer whales (*Orcinus orca*) entering Puget Sound (National Marine Fisheries Service, 2008). A Snohomish County PUD commissioned study on marine mammal use of Admiralty Inlet determined that killer whales may make use of the entire water column during transits. This underscores the possibility that killer whales could come in contact with the proposed tidal turbines. Current plans for monitoring the site include the use of a passive acoustic detection system based on a network of hydrophones in northern Admiralty Inlet. Land-based infrared detection could augment or validate this approach by providing surface images of killer whales as they pass.

The most sightings of Southern Resident killer whales in Puget Sound occur between October and December, however sightings are still relatively rare and difficult to predict (The Whale Museum, 2006). Further north, at Lime Kiln Park, sightings of Southern Resident killer whales are nearly a daily occurrence in June and July. Therefore, Lime Kiln Park was chosen to test the efficacy of land-based infrared detection of Southern Resident killer whales. Figure 1.2 shows the location of Lime Kiln Park in relation to the proposed tidal energy project.

1.2 Electromagnetic Radiation Background

In order to understand the factors that affect infrared imagery it is necessary to understand the fundamentals of electromagnetic radiation (light). Table 1.1 summarizes some important terms used in the description of electromagnetic radiation.

Table 1.1 Electromagnetic radiation terms and definitions. Adapted from Zappa (1994).

Term	Symbol	Definition	Units
Flux	Φ	Energy per unit time	Watt (W)
Flux density	I or M, see below	Flux per unit area	$\frac{W}{m^2}$
Irradiance	I	Flux density incident on a surface/body	$\frac{W}{m^2}$
Exitance or Emmitance	M	Flux density emitting from a surface/body	$\frac{W}{m^2}$
Absorptivity	α	The fraction of irradiance absorbed by a surface	fraction or percent
Reflectivity	ρ	The fraction of irradiance reflected by a surface	fraction or percent
Transmissivity	τ	The fraction of irradiance transmitted through a body	fraction or percent
Emissivity	ε	The ratio of the total power emitted by a surface to the total power emitted from a blackbody at the same temperature	fraction or percent
Incidence angle	θ	Angle between a downward pointing vector (i.e. normal to sea surface) and a given line of sight.	degrees
Zenith Angle	θ_z	Angle between vector pointed at the zenith (directly upward) and a given line of sight.	degrees

Electromagnetic radiation is energy that is transmitted as a stream of photons (massless particles) moving at the speed of light (*c*). Photons travel in a wave-like pattern and oscillate at a frequency (ν) that depends on the amount of energy in each photon. Photon energy (E) and frequency (ν) are related by the Planck-Einstein relation

$$E = h\nu \qquad 1.1$$

where *h* is Planck's constant (6.33 x 10^{-34} J s).

Since all light is moving at the same speed (*c*), the frequency (ν) is directly related to the wavelength (λ), as shown in equation 1.2. High energy photons such as those that make up gamma-rays and x-rays travel with a higher frequency and therefore a shorter wavelength. Lower energy photons such as those that make up television and radio waves have a lower frequency and a corresponding longer wavelength.

$$c = \lambda\nu \qquad 1.2$$

where $c = 2.9979x10^8 m/s$.

1.2.1 The Electromagnetic Spectrum

The electromagnetic spectrum classifies the types of electromagnetic radiation based on frequency or wavelength. As can be seen in Figure 1.3, visible light makes up only a small portion of the full spectrum (0.410 μm ≤λ≤ 0.770 μm). This is the only portion of the spectrum that can be seen by the human eye. Infrared radiation can be felt as heat and makes up 52% of the irradiance of sunlight at sea level (American Society for Testing and Materials, 1992). The infrared spectrum ranges from 0.770 to 100 μm and can be categorized further into near infrared (NIR), short wave infrared (SWIR), medium wave infrared (MWIR), long wave infrared (LWIR), and very long wave infrared (VLWIR), as shown in Table 1.2.

Table 1.2 Infrared spectral bands and primary applications (Maldague, 2007).

Spectral band	Range (µm)	Applications
NIR	0.77-1	Telecommunications
SWIR	1-3	Remote sensing
MWIR	3-5	High temperature inspection (indoors, scientific research)
LWIR	8-14	Ambient temperature (outdoor, industrial inspection)
VLWIR	14-100	Spectrometry, astronomy

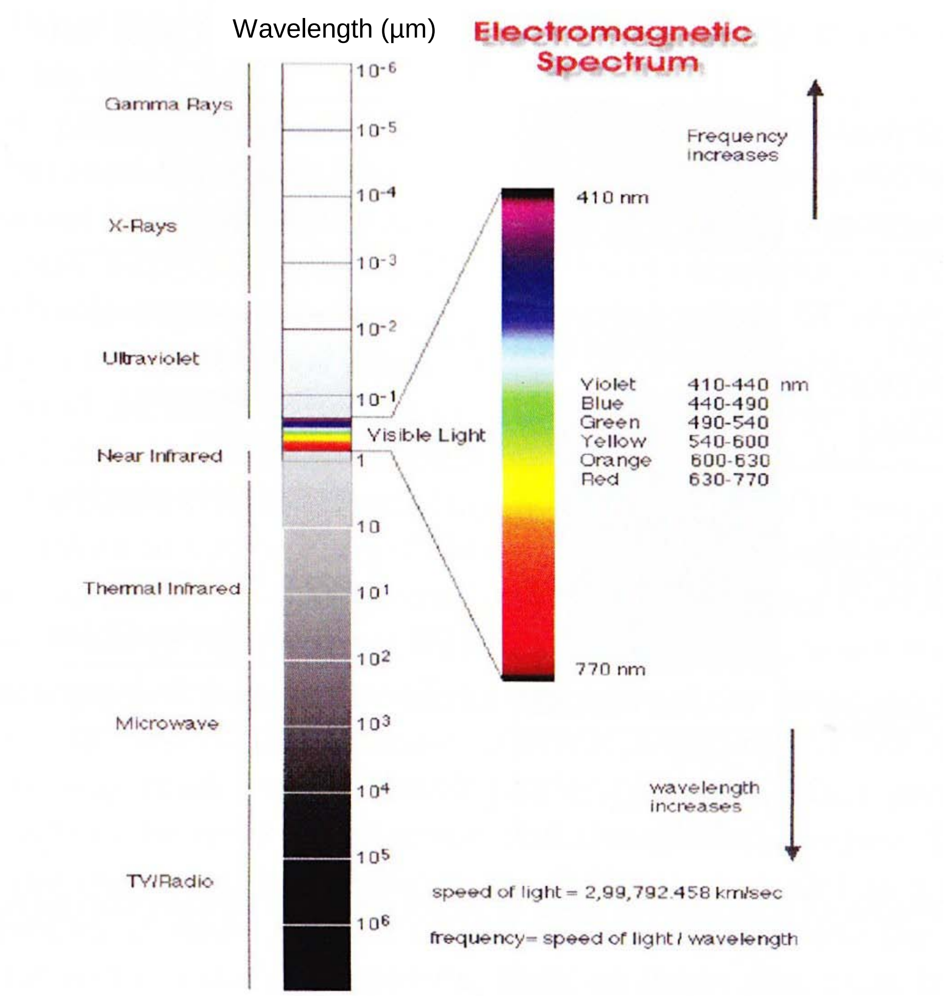

Figure 1.3 Electromagnetic spectrum from Jacobs (2006).

1.2.2 Blackbody Radiation

When radiation reaches a body or surface, a portion of the energy is absorbed (α), a portion is reflected (ρ), and a portion is transmitted (τ). From conservation of energy,

$$\alpha + \rho + \tau = 1. \tag{1.3}$$

Water is translucent (allows some light to pass through, $\tau > 0$) to visible light, however it is essentially opaque ($\tau = 0$) to infrared radiation with wavelengths longer than 3 µm (Zissis, Accetta, & Shumaker, 1993). For opaque bodies ($\tau = 0$), equation 1.3 simplifies to

$$\alpha + \rho = 1. \tag{1.4}$$

When a body or surface is at thermal equilibrium, energy conservation dictates that the energy absorbed must equal the energy emitted. This relationship is the most general form of Kirchhoff's law of thermal radiation and states that at a given wavelength (λ) and direction (θ), the absorptivity (α) must be equal to the emissivity (ε) (Zissis, Accetta, & Shumaker, 1993);

$$\alpha(\lambda, \theta) = \varepsilon(\lambda, \theta). \tag{1.5}$$

Combining equations 1.4 and 1.5 we arrive at

$$\varepsilon(\lambda, \theta) + \rho(\lambda, \theta) = 1, \tag{1.6}$$

which is the standard form of Kirchoff's law.

According to equation 1.3, absorptivity cannot exceed 1 (when ρ = τ =0). Combining this with Kirchhoff's law (1.6) places an upper limit of 1 on emissivity. A body with an emissivity of 1 is known as a blackbody and is both an ideal absorber and an ideal emitter (Jacobs, 2006). The concept of a blackbody is an important tool for the study of electromagnetic radiation. Planck (Jacobs, 2006) was able to show that the spectral radiant emittance (*M*) of a blackbody depends only on the wavelength (λ) and absolute surface temperature (*T*) via Planck's law

$$M_{bb}(\lambda, T) = \frac{2c^2h}{\lambda^5\left[e^{\frac{hc}{\lambda Tk}} - 1\right]}, \qquad 1.7$$

where k is Boltzmann's constant (1.38 x 10^{-23} J/K). Stefan and Boltzmann integrated over all wavelengths to obtain total radiant emittance;

$$M_{bb} = \sigma T^4 \qquad 1.8$$

where $\sigma = 5.67\ x\ 10^{-8}$ and is known as the Stefan-Boltzmann constant (Jacobs, 2006).

For real surfaces, the emissivity (less than 1) is the ratio of the radiation emitted by the surface to the radiation that would be emitted from a blackbody at the same temperature;

$$\varepsilon(\lambda, T) = \frac{M(\lambda,T)}{M_{bb}(\lambda,T)}. \qquad 1.9$$

The temperature associated with $M(\lambda, T)$ is called the apparent temperature (also known as brightness or radiance temperature) and is defined as the temperature of a blackbody that would produce the same spectral radiance as an observed real body. The temperature measured by infrared sensors is an apparent temperature.

Another useful concept is that of a graybody. A graybody is defined as a body whose emissivity is independent of wavelength (ε(λ)=ε). Although the emissivity of most real surfaces are wavelength dependent, graybodies can often be used as an approximation for many natural and manmade materials (Jacobs, 2006). For a graybody, equations 1.9 and 1.8 can be combined to obtain

$$M = \epsilon\, \sigma T^4. \qquad 1.10$$

1.2.3 Emissivity Effects of the Sea Surface

The degree to which the sea surface deviates from a blackbody is highly dependent on incidence angle. For land-based imagery, the incidence angle is determined from the mounting elevation of the camera (h) and the distance to the target (d), as shown in Figure 1.4. In many land-based deployments, the distance to the target is large in comparison to the elevation of the camera, resulting in large incidence angles.

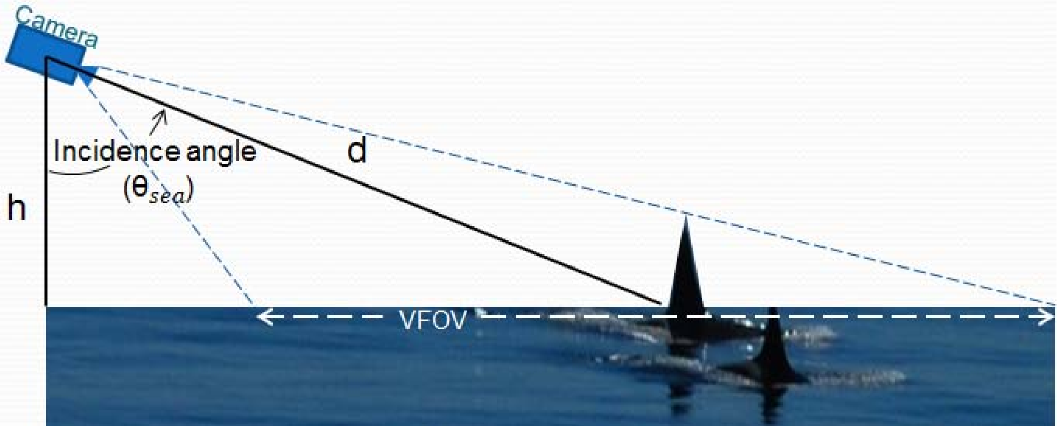

Figure 1.4 Incidence angle geometry, d = distance to target, h = elevation of camera.

$$\theta_{sea} = \cos^{-1}\frac{h}{d} \qquad 1.11$$

The surface of a calm sea will have an emissivity near unity (ε_{sea}=0.98) at near zero incidence angles (i.e., the camera’s line of sight is normal to the sea surface, θ_{sea}□ 0°). As the incidence angle increases to near grazing (i.e., the camera’s line of sight is parallel to the sea surface, θ_{sea}□ 90°) emissivity decreases and the reflection of the sky dominates the signal. Figure 1.5 shows the emissivity and reflectivity of sea water as a function of wind speed and incidence angle. The emissivity remains near unity for angles between 0 and 60°. For angles above 60°, the emissivity decreases rapidly and the corresponding reflectivity increases. As wind speed increases, the sea surface is less reflective due to surface disturbances such as waves, white caps, and foam.

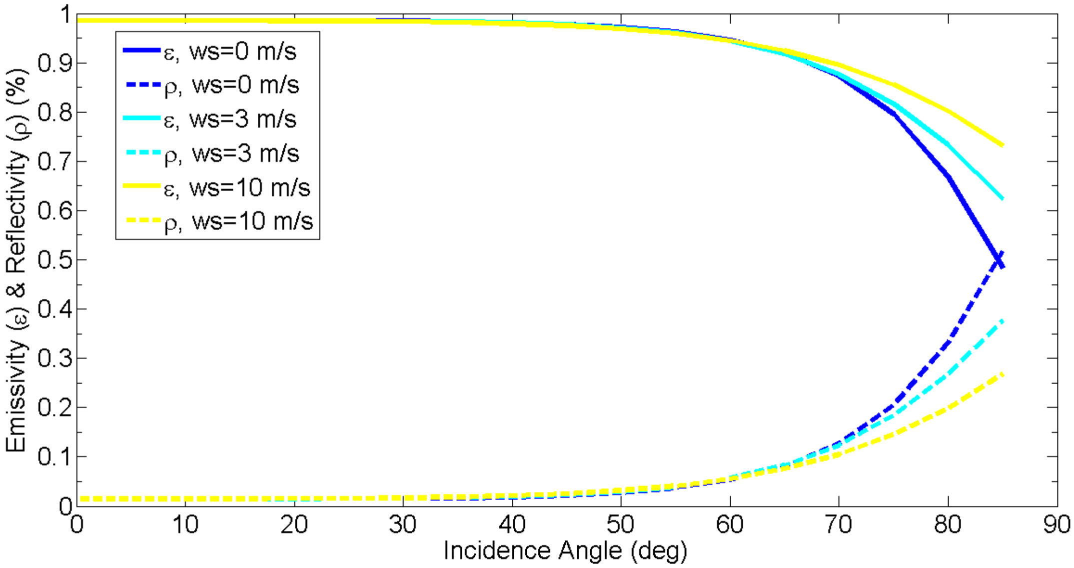

Figure 1.5 The average emissivity (ε) and reflectivity (ρ) for 7 µm <λ< 14 µm as a function of incidence angle for sea water at windspeeds (ws) of 0, 3, and 10 m/s (Filipiak, 2008).

The surface emittance (*M*) recorded by an IR imager is the sum of instrument response-weighted emittance of the sea and the reflected irradiance of the sky;

$$\mathrm{M} = \frac{\int_{\lambda_1}^{\lambda_2} \varepsilon(\lambda, \theta_{sea})\mathrm{R}(\lambda)(\mathrm{M}_{sea}(\lambda, T_{sea})\,\mathrm{d}\lambda}{\int_{\lambda_1}^{\lambda_2} \mathrm{R}(\lambda)\,d\lambda} + \frac{\int_{\lambda_1}^{\lambda_2} \rho(\lambda, \theta_{sea})\mathrm{R}(\lambda)\mathrm{M}_{sky}\left(\lambda, T_{sky}\right)\mathrm{d}\lambda}{\int_{\lambda_1}^{\lambda_2} \mathrm{R}(\lambda)\,d\lambda} \quad 1.12$$

where $\mathrm{M}_{sea}(\lambda, T_{sea})$ is the spectral emittance of the sea at temperature T_{sea}

$\mathrm{M}_{sky}\left(\lambda, T_{sky}\right)$ is the spectral emittance of the sky at temperature T_{sky}

$\mathrm{R}(\lambda)$ is the instrument response

$\varepsilon(\lambda, \theta_{sea})$ is the sea surface spectral emissivity

$\rho(\lambda, \theta_{sea})$ is the sea surface spectral reflectivity.

Figure 1.6 shows the dependence of sea surface emissivity (ε) on wavelength at incidence angles from 0° to 80°, as well as the spectral response of the FLIR A40M used in this study.

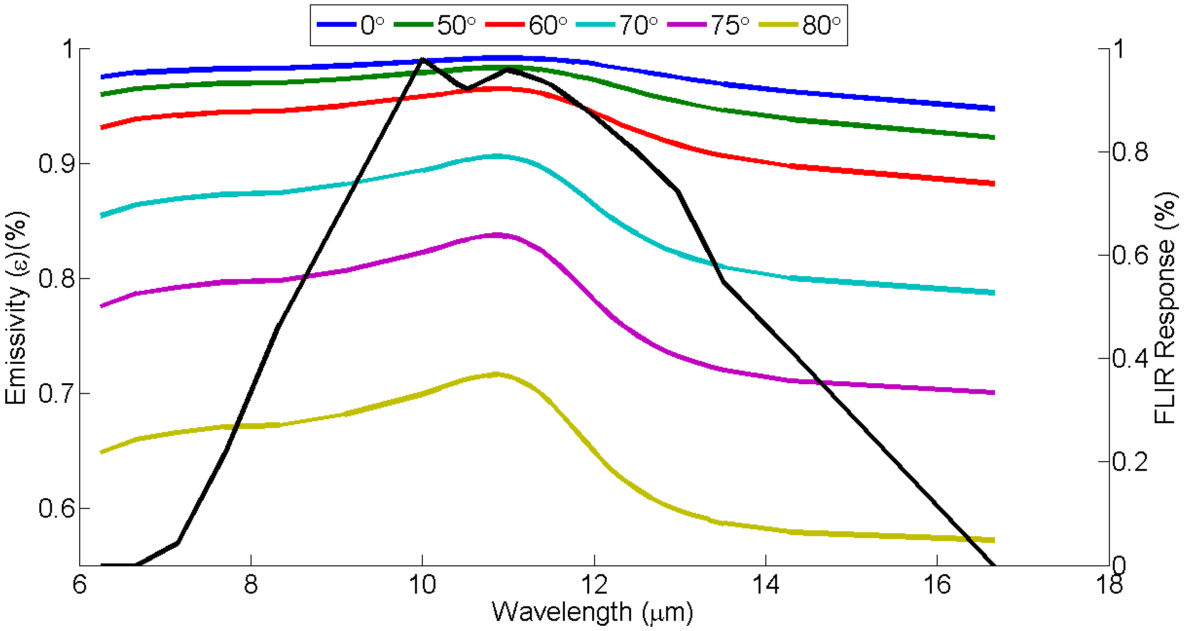

Figure 1.6 Sea surface emissivity versus wavelength at incidence angles from 0° to 80° and wind speed of 0 m/s. The spectral response of the FLIR A40M is also shown. Emissivity data from Filipiak (2008).

It can be seen that the spectral dependence of emissivity is small in relation to the dependence on incidence angle. If graybody behavior is assumed within the bandwidth shown, the effective band emissivity $\varepsilon_{eff}(\theta_{sea})$ from λ_1 to λ_2 can be calculated from

$$\varepsilon_{eff}(\theta_{sea}) = \frac{\int_{\lambda_1}^{\lambda_2} \varepsilon(\lambda,\theta_{sea})\mathrm{R}(\lambda)\, d\lambda}{\int_{\lambda_1}^{\lambda_2} \mathrm{R}(\lambda)\, d\lambda}. \qquad 1.13$$

Combining equations 1.12 and 1.13 yields

$$\mathrm{M} = \varepsilon_{eff}(\theta_{sea})\mathrm{M}_{sea}(T_{sea}) + \rho_{eff}(\theta_{sea})\mathrm{M}_{sky}(T_{sky}). \qquad 1.14$$

In summary, sea surface emittance (*M*) is a combination of the emitted radiation from the sea and the reflected radiation from the sky (Jessup & Branch, 2008). Therefore, the sea surface temperature seen by an infrared imager (apparent temperature) has a dependency on both the true sea temperature and the sky temperature. At large incidence angles, this dependence increases as reflectivity dominates over emissivity.

A clear, dry sky can behave like a blackbody emitter with a temperature as low as -60 °C (Jessup, 2004). With these conditions, an IR image taken at a large incidence angle would be expected to show an apparent temperature lower than the true temperature of the water. The image in Figure 1.7 shows the effects of sky reflection on an IR image. The incidence angle increases from the bottom (58°) to the top (85°) of the image and the corresponding apparent temperature decreases.

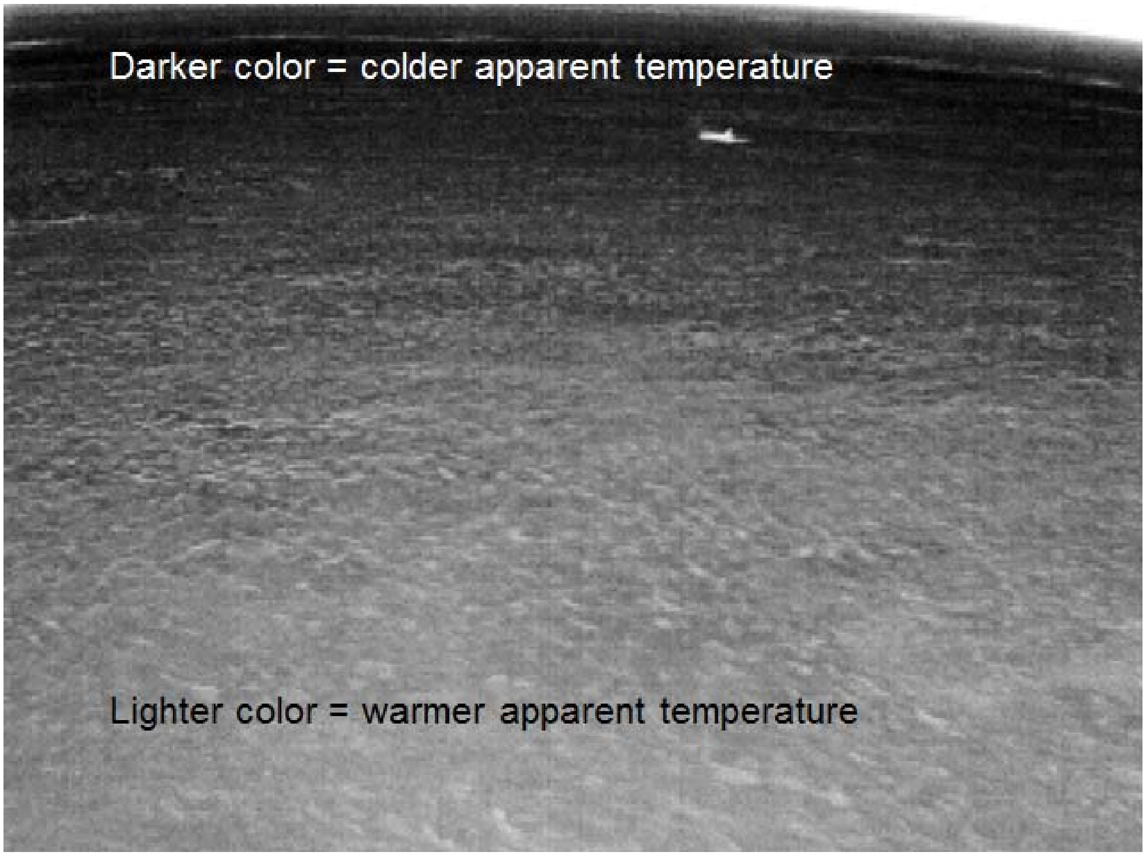

Figure 1.7 **An example of emissivity effects of the sea surface. The area at the bottom of the image has a lower incidence angle and appears warmer (lighter) than the top of the image due to less reflection of the sky temperature. A whale can be seen surfacing in the far-field.**

This reduction in the apparent temperature is important to marine mammal detection since marine mammals are well insulated and their surface temperature does not vary greatly from the surrounding water. In addition, the mammal’s skin can remain covered in a thin film of water during the duration of the surface (Cuyler, Wiulsrod, & Oritsland, 1992). When a killer whale (or similar cetacean species) surfaces, its body, dorsal fin, and blow all protrude above the sea surface. Figure 1.8 shows these three possible detection targets.

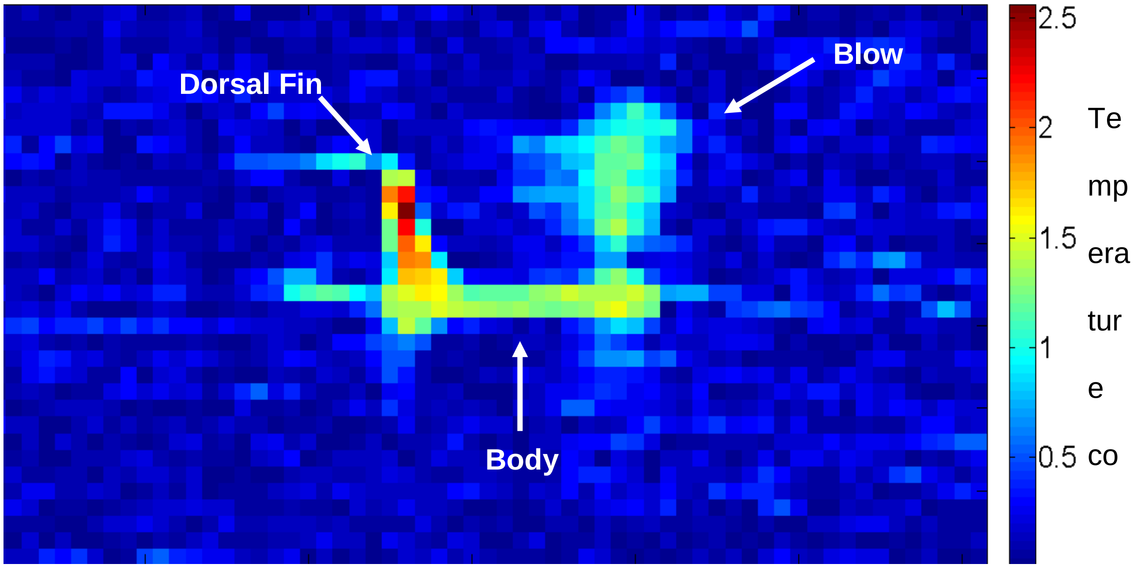

Figure 1.8 Infrared image of potential targets for cetacean detection. Color map has been adjusted to enhance visual contrast. Color bar shows temperature contrast from the sea surface mean (°C).

Blows can range between 1 and 5 meters tall depending on weather conditions. At long distances, blows are the easiest target to detect because of the relatively large size and height above the sea surface. During windy conditions, blows can appear nearly horizontal and can be confused with the sea surface (Perryman, Donahue, Laake, & Martin, 1999). The body size of a female killer whale averages from 4.9 to 5.8 meters and males average from 5.8 to 6.7 meters (SeaWorld Parks & Entertainment, 2011). However, during normal activity very little of the whale’s body protrudes above the sea surface, so it is a poor target for detection or tracking.

Killer whales have the largest dorsal fins of all cetaceans ranging in size from 0.9 to 1.8 meters (SeaWorld Parks & Entertainment, 2011). From the three potential detection targets shown in Figure 1.8, the dorsal fin is the only one with a fairly predictable relative angle to the sea surface. Although the angle between the fin and sea surface varies from fin to fin, they remain relatively close to 90°.

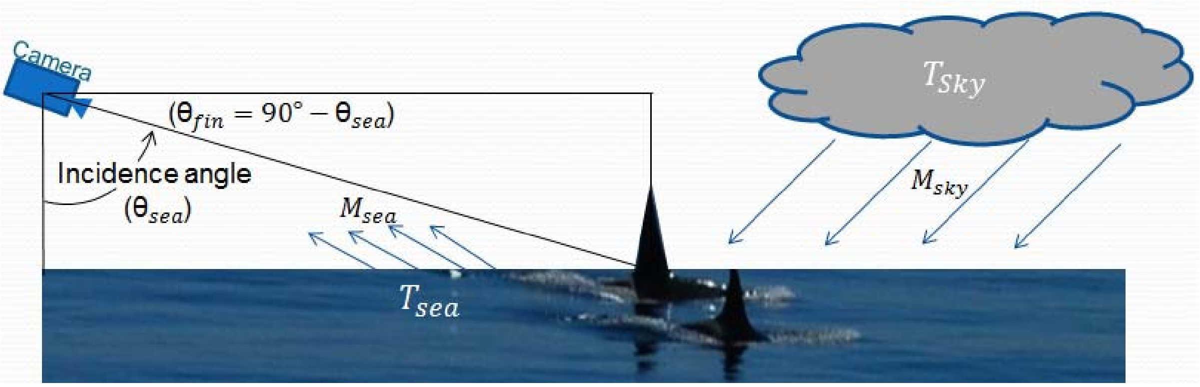

Figure 1.9 The incidence angle to a protruding dorsal fin is much smaller than the incidence angle to the sea surface when θ_{sea} is large.

$$\theta_{fin} = 90° - \theta_{sea} \qquad 1.15$$

As shown in Figure 1.9, for large incidence angles ($\theta_{sea} > 60$), the angle from the camera to a protruding dorsal fin (equation 1.15) is near nadir. Assuming the dorsal fin is covered with a film of sea water, it would be expected to have similar emissivity properties as that of water. The estimated range of emissivities for the sea surface and dorsal fin are shown in Figure 1.10. The fin will have an emissivity near unity while the emissivity of the sea surface decreases rapidly above 60° incidence angle. The incidence angles shown in Figure 1.10 are derived from IR images that are described in more detail in Chapter 2. As the emissivity of the sea surface decreases, more of the received signal depends on reflection from the sky. Since the emissivity of a protruding fin remains fairly constant, the temperature contrast between the fin and the surrounding water would be expected to increase with incidence angle.

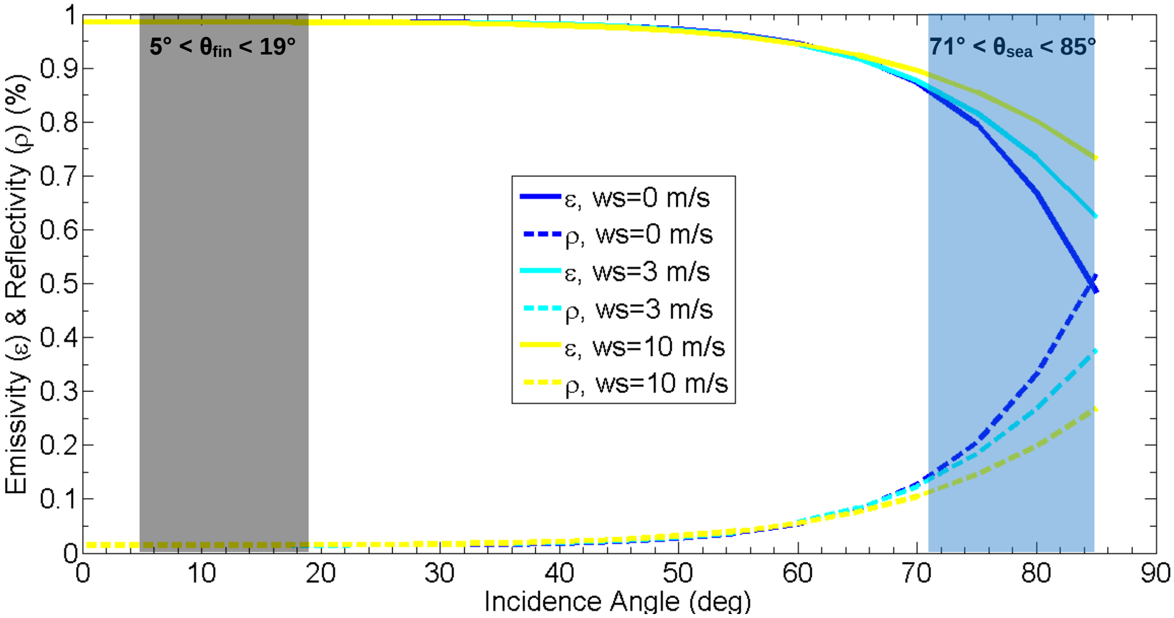

Figure 1.10 The range of emissivity (ε) and reflectivity (ρ) from a protruding dorsal fin (θ_{fin}) and the sea surface (θ_{sea}).

1.3 Infrared Camera Technology

Advancements in infrared camera technology, based on microbolometers that are sensitive to long wave infrared (LWIR) in the 7-14 μm wavelengths, have enabled a new generation of IR cameras that are small, light, and relatively inexpensive ($5k - $100k). The main limitation of uncooled microbolometer cameras are increased noise levels and signal drift with temperature change. Traditional infrared cameras are based on photovoltaic detectors that must be cooled with liquid nitrogen to maintain a constant temperature and reduce thermal noise. The inherent noise level of a camera is indicated by the noise equivalent temperature difference (NETD). NETD is a measurement of the internal noise given in units of temperature. A typical NETD value for cooled cameras is 25 mK, while uncooled cameras range from 50-150 mK. Frequent non-uniformity correction (NUC) (approximately hourly) is required to maintain low levels of noise during changes in ambient temperature for microbolometer-based IR cameras. The NETD range of microbolometer cameras allows detection of temperature differences in the field as low as 100 mK (Jessup, Chickadel, & Stafford, 2009). Previous studies have shown that this sensitivity is sufficient for marine mammal detection (Baldacci, Carron, & Portunato, 2005; Cuyler, Wiulsrod, & Oritsland, 1992; Perryman, Donahue, Laake, & Martin, 1999). The increased availability of relatively inexpensive microbolometer-based cameras provides an opportunity for marine mammal observation in the infrared spectrum. The remainder of this study addresses the optical, geometric, and environmental parameters that should be considered for the deployment of an infrared camera for this purpose.

1.4 Previous Studies

Cuyler et al. (1992) published one of the first studies using infrared imagery to observe marine mammals. A liquid nitrogen cooled AgemaThermovision 880 imaging system (8-12 µm IR sensitivity, 7° field of view (FOV), 280x175 pixel resolution) was mounted on a boat 8 meters above sea level. Temperature contrasts of minke, humpback, fin, blue and sperm whales were measured at close ranges (10-70 meters). The observations were collected off the northern coast of Norway and the northwest coast of Svalbard during a three week period in July 1989. Air temperature ranged from 2.5 to 13 °C and sea surface temperature ranged from 2.7 to 10.1 °C. The weather was overcast with mostly calm seas and winds. Emissivity effects were observed with incidence angles above 60°. Cuyler et al. reported that detection was “enhanced” since whale surfaces incorrectly appeared 0.5 to 1.0 °C warmer than the sea surface immediately surrounding them. Consequently, temperature values for the sea and whale surface with incidence angles greater than 60° were disregarded. For the remaining measurements, the sea surface emissivity, whale surface emissivity, and blow emissivity were kept constant at 0.96. Due to the close proximity to the whales during observation, the main contributions of this study are field measurements of the temperature contrast between whales (blow, body, and appendages) and the surrounding sea surface (Jessup, Chickadel, & Stafford, 2009). The whales' bodies showed the lower temperature contrasts than their blows or appendages. Minke whales showed the lowest contrast between body and sea temperature, with a maximum value of 0.1°C. For other species, the contrast ranged up to 1 °C. The contrast for appendages such as fluke, flipper, and dorsal fins were shown to range between 0.5 and 1.9 °C for minke, humpback, and fin whales and as high as 6 °C for sperm whales. The temperature contrast between the blow and the surrounding water ranged from 0.3 to 4 °C for all species. Cuyler et al. concluded that the detection of whales by thermal infrared from the body trunk appeared unreliable and suggested instead to use the blow and blowhole. For the entirety of the study, all the whales were sighted visually before the infrared detector was turned on, so direct detection using infrared imagery was not demonstrated (Cuyler, Wiulsrod, & Oritsland, 1992).

The most extensive land-based study to date was conducted by Perryman et al. (1999) tracking the migration of gray whales from the Granite Canyon Research Station near Carmel, California. They used an AN/KAS-1A military thermal imaging system with a cooled long wave infrared sensor (LWIR, λ= 8-12μm). The sensor had a 3.4° x 6.8° field of view (FOV) and 3 x magnification. Observations were taken in January for three consecutive years (1994-1996) and coincided with the National Marine Mammal Laboratory’s (NMML) yearly visual survey. One sensor was used in 1994, and a second, adjacent sensor was added in 1995 and 1996. The sighting distance ranged from 0.5 to 5.4 km and yielded an average migration path of 2 km. Perryman et al. reported that whale blows were clearly visible both night and day. However poor weather, such as high winds, fog, and rain decreased the probability of detection. Data included in the study conclusions were obtained only during “very good” or “excellent” weather conditions. Weather conditions were categorized based on how easily a whale blow could be seen. “Excellent” weather was defined as calm seas, light wind, and blows that appeared as persistent columns. “Very good” weather was described as having some small waves, light wind, and blows that were less persistent, but clearly visible. During periods of moderate winds with whitecaps (“Good” weather rating) blows mixed rapidly and were sometimes indistinguishable from white caps. With moderate seas and swells (“Fair” weather rating) blows were horizontal and were lost in the confusion of the sea surface (Perryman, Donahue, Laake, & Martin, 1999).

Although adequate for the described study, the ratings used are qualitative and cannot easily be translated into the maximum allowable sea state for possible infrared detection. Table 1.3 shows the World Meteorological Organization’s (WMO) sea state categories and corresponding wave heights. Perryman et al. describe moderate winds with whitecaps as a “Good” weather rating, which might be loosely translated as WMO sea state 4.

Table 1.3 WMO Sea State categories by wave height.

WMO SEA STATE	WAVE HEIGHT (M)	CHARACTERISTICS
0	0	Calm (glassy)
1	0 to 0.1	Calm (rippled)
2	0.1 to 0.5	Smooth (wavelets)
3	0.5 to 1.25	Slight
4	1.25 to 2.5	Moderate
5	2.5 to 4	Rough
6	4 to 6	Very rough
7	6 to 9	High
8	9 to 14	Very high
9	Over 14	Phenomenal

During daylight hours, visual observations were conducted concurrently with the infrared imagery. Unlike Cuyler et al., the infrared camera continued recording during the entire survey period, regardless of visual detections. The infrared footage was later reviewed to detect and track whale blows. Comparisons of visual and infrared counts during the day showed that the two methods produced comparable results (Perryman, Donahue, Laake, & Martin, 1999).

From August to September 2003, Baldacci et al. (2005) used SAGEM MATIS IR binoculars (3-5 μm sensitivity, 9°x6° or 3°x2° FOV, 384x256 pixels) to detect a variety of dolphin and whale species from two NATO vessels off the west coast of the Italian islands of Sardinia and Corsica. Air temperature varied between 25 and 29 °C and humidity varied between 85 and 95%. As with Cuyler et al., visual binoculars were used for initial detection, so there were no detections recorded at night. Baldacci et al. reported that IR was ineffective with sea state greater than 2 or 3. It was also reported that the IR system was ineffective in the presence of high humidity, but “high” humidity is not quantified. The detection range varied from 0.5 to

8.8 km. Blows were the primary feature identified, however the fluke and skin were also visible (Baldacci, Carron, & Portunato, 2005).

Studies by Schoonmaker et al. (2008), and Podobna et al. (2010) focused primarily on multispectral imaging and involved instrumentation purpose-built for marine mammal detection. In 2008, a device called the MANTIS 4 was tested along with an infrared (8-12 µm sensitivity, no additional information provided) and digital video camera. The system was mounted on a cliff (elevation not provided) in Maui Hawaii. Schoonmaker et al. reported infrared detection of mammals at both day and night at ranges up to 8 miles. In 2010, a device called EYE5 was tested in an airborne survey of humpback whales over Maui, Hawaii. The EYE5 system includes 3 multispectral cameras (400-850nm, 5.5°-50° FOV depending on lens, 1392 x 1024 pixels), a ThermoteknixMiricle 307K IR camera (7-14µm, 37° FOV, 640 x 480 pixels), and a Sony digital camera. The system includes target tracking and integrated foveal view. The term “foveal vision” refers to a system that allows for both wide angle viewing and the ability to zoom in on an identified target (Jessup, Chickadel, & Stafford, 2009). In the case of EYE5, the infrared and digital video cameras are used to capture high resolution images of a target identified by the multispectral cameras. Designed primarily for daytime airborne surveys, the multispectral cameras are shown to detect whales beneath the water’s surface, although there is no independent measurement of their depth.

Chapter 2 - Field Observations

2.1 Instrumentation

2.1.1 Cameras

Infrared and visual imagery were collected at Lime Kiln Park, Washington from 7/6/10-7/9/10. Three cameras were mounted to the railing of the Lime Kiln Park lighthouse (Latitude 48°30'57"N Longitude 123° 9'9"W) at a height of 13 meters above sea level. The cameras were positioned to face West towards Victoria BC with an incidence angle of 72°. The horizon was just visible at the top of the field of view.

Table 2.1 Cameras used at Lime Kiln Park.

Camera	Sensor Type	Resolution (Pixels)	Focal Length	Data Out
FLIR Thermo Vision A40M w/wide angle lens	Focal Plane Array (FPA), uncooled microbolometer	320 x 240	18 mm (Fixed)	IEEE 1394
Canon VB-C50FSi	Canon 1/4” CCD	640 x 480	3.5mm – 91 mm	CAT5 (POE hub)
Flea2 FL2-08S2M	Sony ICX204 1/3” CCD	1032 x 776	4 mm (Fixed)	IEEE 1394

The infrared camera used is a FLIR ThermoVision A40M with an 18 mm lens (7.5-14µm, 37° horizontal field of view, 320x240 pixels). The FLIR A40M uses an INDIGO sensor with an NETD of 0.05 °C. Image non-uniformities due to sensor drift were removed using the built in, non-uniformity correction (NUC) function. The FLIR A40M NUC function mechanically positions an internal blackbody in front of the sensor. Camera software then automatically identifies and corrects for non-uniformities. The camera software corrects for lens temperature drift using a lens-specific look-up table. The lookup table is created through laboratory testing at FLIR before the unit is delivered and is unique to each individual lens. For daytime recordings, a NUC correction was made at the start of each marine mammal detection. Due to limited access to the equipment at night, no NUC corrections were completed during nighttime recordings, resulting in significant noise from temperature drift. This noise was removed by using post-processing techniques discussed in section 2.4.

Two visual cameras based on charge-coupled devices (CCDs) were mounted to the same housing as the FLIR A40M. A Canon VB-C50FSi was used primarily to test the infrared sensitivity of a CCD-based camera for night filming. CCDs are sensitive to visible (410-770 nm) as well as near infrared (NIR, 770-1400 nm) wavelengths. To avoid recording an image that differs from what can be seen visibly; most CCD-based digital cameras include an infrared cut filter to cut out the NIR wavelengths. The Canon VB-C50FSi includes a night mode setting that mechanically removes the interior infrared cut filter from the camera’s line of sight. Even with the infrared filter removed, detection was not possible using the Canon before nautical dawn or after nautical dusk, as discussed in section 4.1.

The third camera used is a Point Grey Research FLEA2 FL2-08S2M used to collect high resolution black and white images during day recordings.

Figure 2.1 The mounting location and geometry for the cameras at Lime Kiln Park.

As shown in Figure 2.1, the Canon VB-C50FSi was mounted side by side with the FLIR camera and the FLEA was mounted under the camera housing. The front acrylic glass was removed from the protective housing to avoid attenuation of the IR signal by the glass.

2.1.2 Ancillary Equipment

Two laptops were used to record the footage. Laptop 1 was loaded with Streams 5 software and connected via IEEE1394 (FireWire) to a FireNEX-CAT5-S400 repeater. The repeater was connected via a 100 ft CAT5 cable to a 2nd repeater which splits the signal from the CAT5 back to two IEEE1394 cables that were connected to the FLIR A40M and FLEA2. Streams 5 software recorded both the output from FLIR A40M and FLEA2 cameras at 7.5 fps. Laptop 2 was connected via CAT5 cable to a TrendNet 8 port power over Ethernet (POE) hub. The POE hub was connected to the Canon VB-C50FSi. LuxRiot DVR software was used to record the output from this camera at 5 fps.

Additional imagery was collected at the proposed tidal energy site in Admiralty Inlet. The Canon VB-C50FSi camera is mounted on the Admiralty Head Lighthouse (Latitude 48° 9'39"N Longitude 122°40'52"W) at an altitude of 38 meters above sea-level (at the top of the 9 meter lighthouse tower). The camera is pointed 210° S to look directly at the proposed tidal energy site. The zoom is fixed at 11.34 mm focal length to capture the full width of Admiralty Inlet, with the horizon in the far-field of view. Footage from the Admiralty Head Lighthouse camera is used to evaluate the performance of a visible spectrum camera under adverse atmospheric conditions.

2.2 Climate

Ideal conditions for visual and infrared observation occurred throughout the field study at Lime Kiln Park with clear skies, air temperatures between 10 and 27 °C, and wind speeds below 4 m/s. As shown in Figure 2.2, global solar radiation was virtually uninterrupted during daylight hours indicating little or no cloud cover. During nighttime hours, the relative humidity reached a maximum of 85% and dropped to a minimum of 43% during the warmest part of the day.

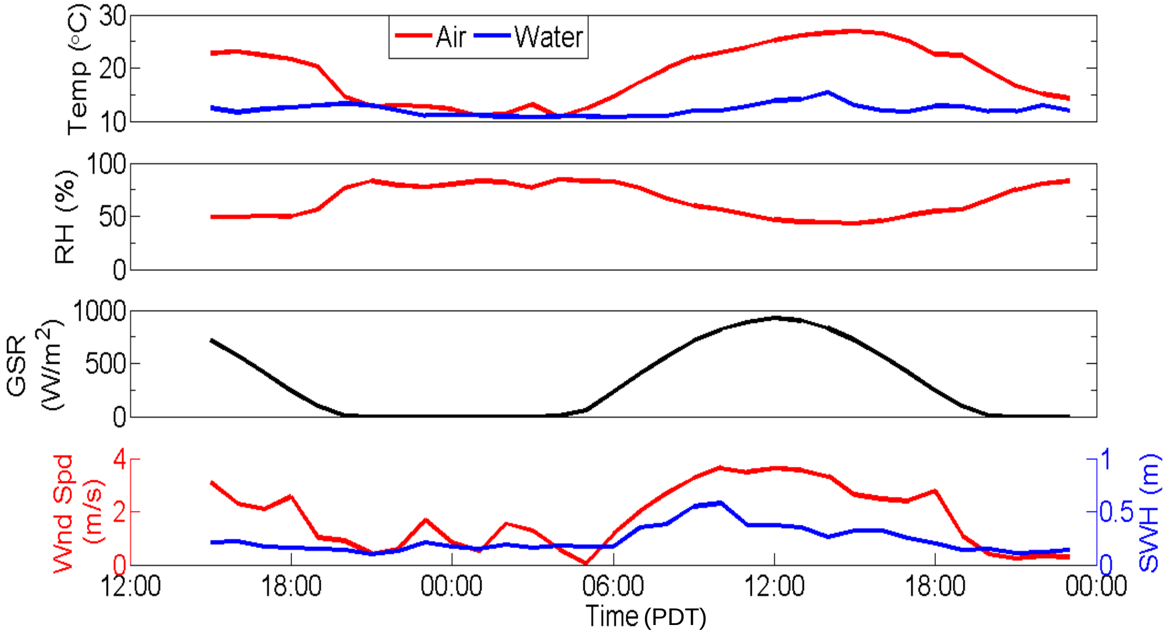

Figure 2.2 Climate data from 7/6 at 15:00 (PDT) through 7/7. Air temperature, relative humidity (RH), global solar radiation (GSR), and wind speed (Wnd Spd) are obtained from WSU AgWeatherNet Whidbey Island Station. Signification wave height (SWH) and water temperature are obtained from NOAA National Data Buoy Center (NDBC) New Dungeness buoy.

2.3 Southern Resident Sightings Summary

During the four days of field observations, Southern Resident killer whales passed Lime Kiln Park 11 times, as shown in Table 2.2. During daylight hours the recording on all cameras was initiated by reports of whales in the area by the Orca Network or the Whale Museum's hydrophone array. The Whale Museum also used this information to make species and pod identifications. Nighttime footage was recorded throughout the night and reviewed the next morning. All eight of the passes (2 nighttime, 3 during twilight, and 2 daytime) on July 7th were captured by the IR camera. The 3 passes on July 8th were not captured. For the pass at 13:57, the whales entered the field of view, but were too far from the camera to be visible in the images. For the passes at 15:13 and 20:37, the whales were near the park and were visible with binoculars, but they never entered the field of view of the camera.

A “surfacing event”, as reported on Table 2.2, is counted each time a single whale can be seen above the surface, and a “pass” is a collection of continuous surfaces with no gaps (where no whales can be seen in the footage) longer than 1 minute . If the same whale surfaces multiple times in the field of view of the camera, this counts as multiple surfacing events.

Table 2.2 Summary of whale passes observed at Lime Kiln Park from July 6th – July 9th 2010.

Day	Start Time (PDT)	Day/Night	Duration (seconds)	Surfacing events captured on IR	Range (meters)
July 7th 2010	3:48	Night	151	22	42-66
July 7th 2010	3:53	Night	25	3	70-82
July 7th 2010	3:57	Night	44	7	106-111
July 7th 2010	4:59	Twilight	72	23	124-162
July 7th 2010	5:10	Twilight	46	20	52-78
July 7th 2010	11:45	Day	40	4	90-128
July 7th 2010	19:25	Day	33	3	84-97
July 7th 2010	19:46	Day	76	2	97-107
July 8th 2010	13:57	Day	N/A	NONE	Out of camera range
July 8th 2010	15:13	Day	N/A	NONE	Not in FOV
July 8th 2010	20:37	Day	N/A	NONE	Not in FOV

2.4 Post-processing

Footage was first reviewed to identify whale sightings. Sections of video with whales were exported from Streams 5 to 16 bit binary format (.raw). The binary files were then read into MATLAB for analysis. Footage of whales was separated into sections of 3 minutes or less (<1350 frames) to enable efficient processing. To identify stationary pixels (due to sensor or lens drift), the mean image was calculated by taking the mean pixel value over all frames within each section. The mean image was then removed from each frame, resulting in an image corrected for drift in the mean. Care was taken to ensure each section of footage has at least 200 frames without whales, so the mean image is not significantly biased by the temperature increase associated with whales surfacing. The pixel value of the corrected frames was then translated from “counts” (cts) associated with the FLIR’s raw signal to temperature contrast (°C) by using the calibration equation (2.1). This equation is camera specific and is derived from laboratory measurements. Figure 2.3 shows a plot of the calibration measurements for the FLIR A40M used in this study.

$$\Delta T = cts/95.2 \tag{2.1}$$

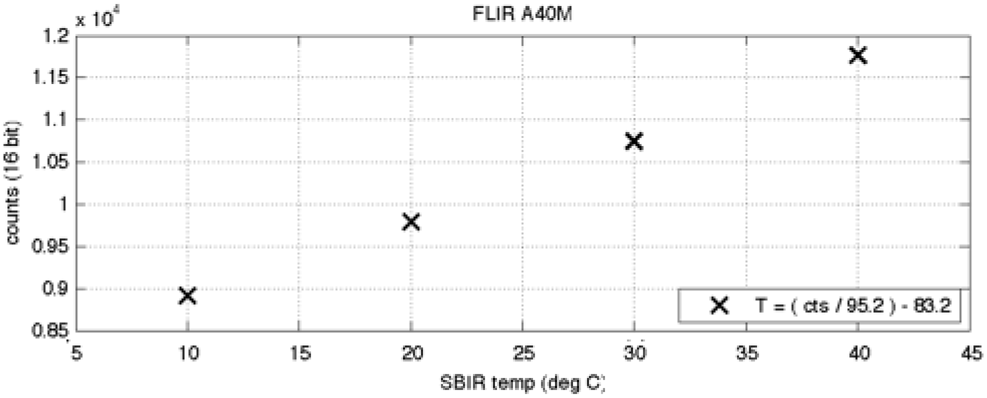

Figure 2.3 FLIR A40M calibration measurements for converting raw counts (cts) into °C (Thomson, unpublished, 2007).

In Figure 2.4, two frames from the early morning passes on July 7th are shown in different stages of post-processing. Since NUC corrections were not completed during overnight recordings, these passes have the highest level of noise due to sensor and lens drift. The raw images are shown exactly as they are recorded. The corrected images are created by first removing the mean image and then changing the color map from gray scale to color to emphasize the contrast. These steps enhance the visibility of whales and surface anomalies (e.g. waves that persist after a whale surfaces).

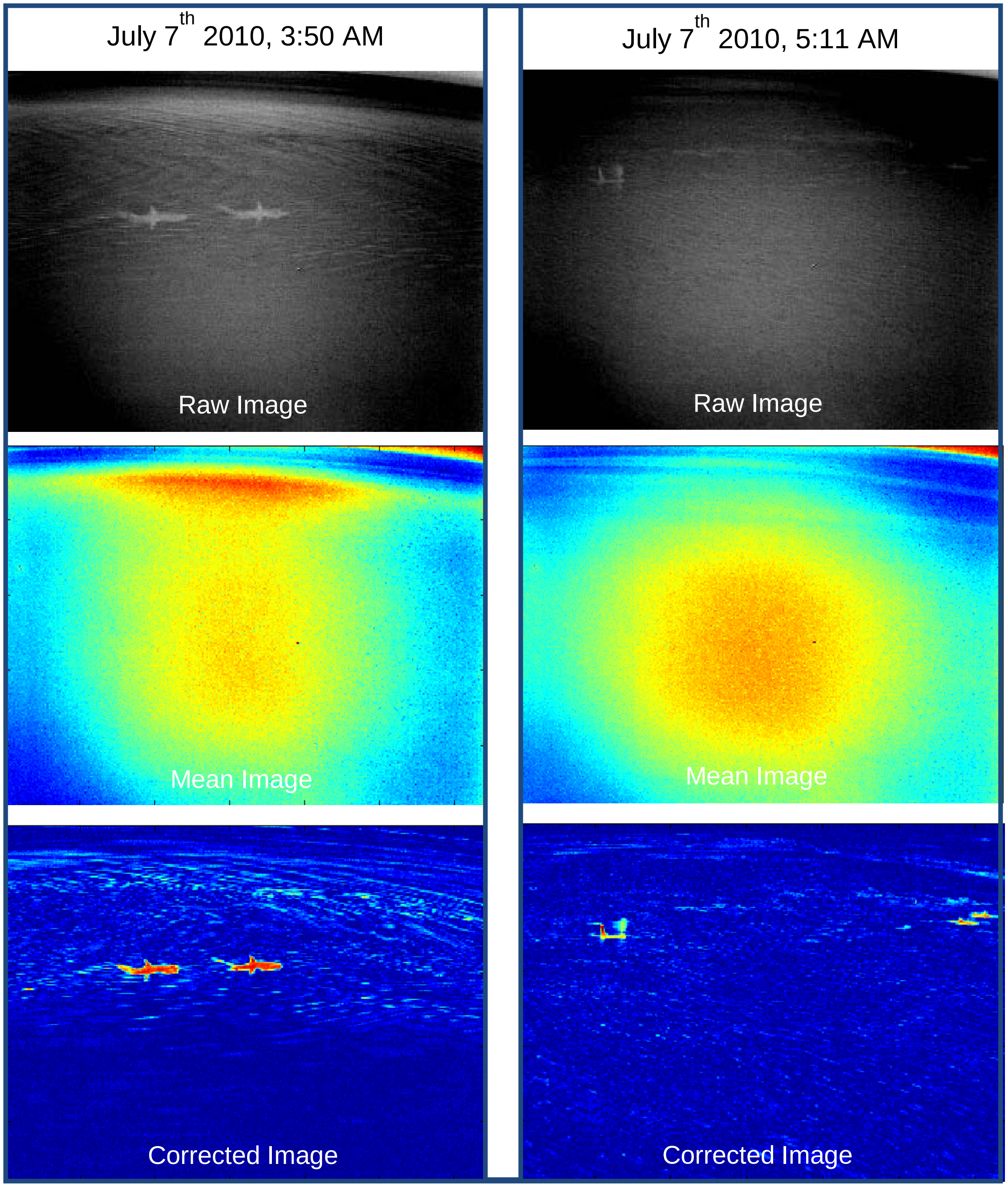

Figure 2.4 An example of post-processing for the early morning passes on 7/7. The mean image is calculated and removed to create the "corrected" image.

As discussed in section 1.2.3, the dorsal fin is the potential detection target with the most consistent angle relative to the sea surface. Once the mean image was removed, the corrected images were manually reviewed frame by frame to identify dorsal fins. The location of each identified fin is recorded by the vertices of a bounding triangle. The accuracy of each bounding triangle was then rated. A rating of “1” indicates that a dorsal fin is clearly distinguishable and the bounding triangle fits the fin well. A rating of “2” indicates that at least a portion of the dorsal fin is distinguishable and the bounding triangle identifies that portion. A rating of “3” indicates that the dorsal fin could not be clearly distinguished, either from the sea surface or the rest of the whale’s body.

Figure 2.5 shows the bounding triangles of all identified fins (624 total) in the camera’s field of view. The color of the triangle indicates the confidence rating discussed above. The ratings vary by surfacing event. However, once the pixel size exceeds 0.12 meters, all fins are rated as either 2 (yellow = fair) or 3 (red = poor) and as pixel size increases to 0.2 meters all fins are rated as 3 (red = poor).

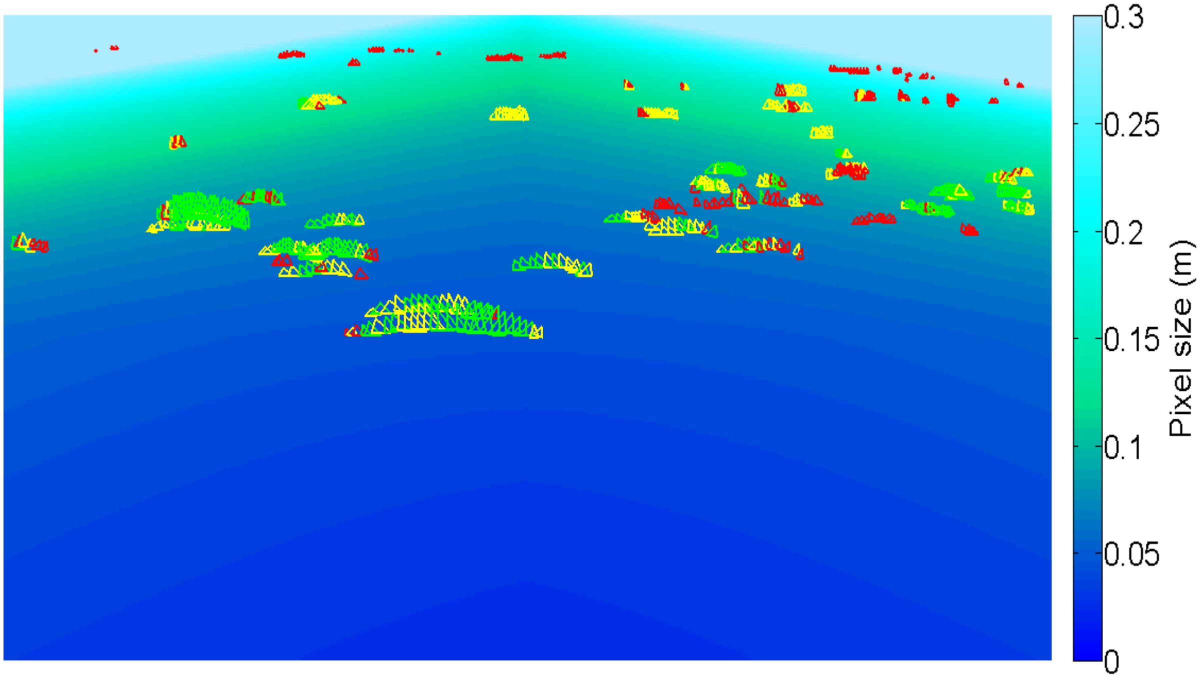

Figure 2.5 The location and rating of all dorsal fins detected as seen in the camera's field of view. The color outline of each fin denotes the confidence rating of fin bounding triangle, 1 (good) = green, 2 (fair) = yellow, 3 (poor) = red. The color gradient indicates pixel size in meters, as defined by the color bar.

2.5 Range

The effective range of an infrared camera depends on the camera’s resolution, field of view, and the size of the desired target. A camera with a given resolution (for example 320 x 240) with a narrow field of view will have a longer range than one with a wider field of view. The camera used for this study has a resolution of 320 x 240 pixels and a 37° horizontal field of view. As shown in Figure 2.5, with this camera geometry whale fins were positivity identified (confidence rating of 1) up to a pixel size of 0.12 m. Figure 2.6 shows the camera’s field of view mapped onto Cartesian coordinates (X-axis facing west, Y-axis facing south) (Holland, Holman, Lippmann, Stanley, & Plant, 1997). It can be seen that all fins with a confidence rating of 1 (green) fall within a 75 meter range. This suggests a maximum distance of 75 meters for identifying killer whale fins with this particular camera and lens geometry. Pixels size is larger on the edge of the field of view due to radial lens distortion. Distortion varies by lens and is more prominent in wide angle lenses such as the 37° FOV lens used in this study.

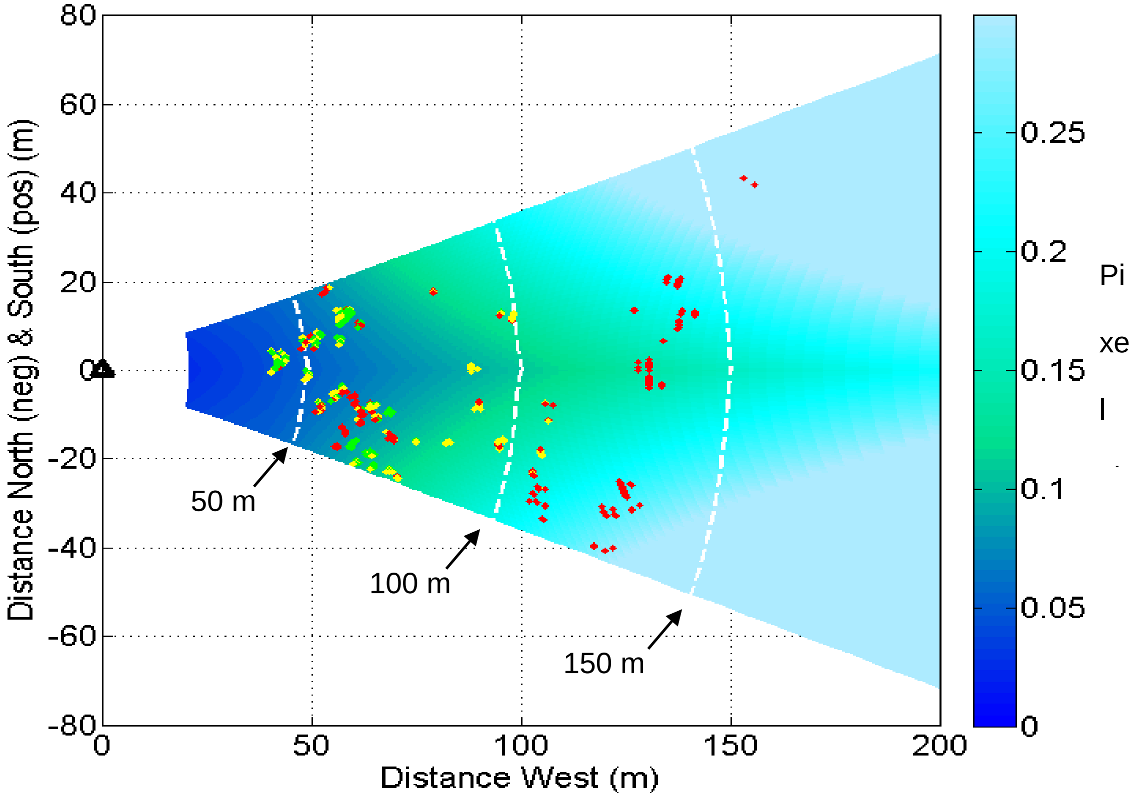

Figure 2.6 FOV of FLIR A40M (320 x 240 resolution, 37° FOV) camera at Lime Kiln Park in real world coordinates. Axes show distance from camera, the X-axis shows distance west and the Y-axis shows distance south (positive) and north (negative). Contours (white dotted lines) show line of sight distance to camera. Color gradient denotes pixel size (m)

Figure 2.7 shows examples of identified fins at increasing distances from 43 to 162 meters to illustrate the difficulty of identifying fins at long distances. At distances of 43 and 61 meters, fins can be easily distinguished from the body. However, as the distance increases to 90 meters, the fin is difficult to distinguish. At 162 meters a single pixel includes the whole whale (fin and body) making it impossible to distinguish between the two.

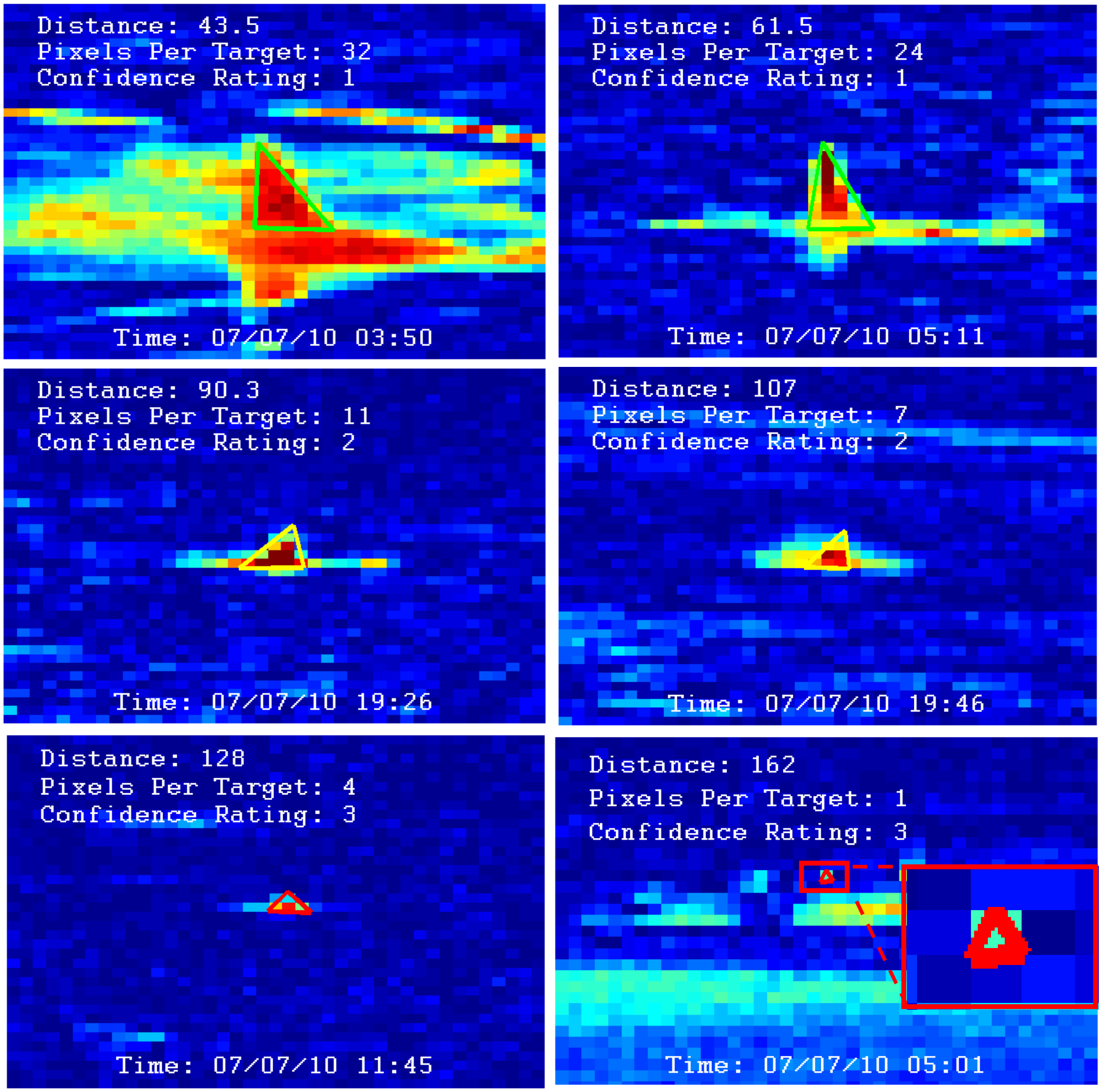

Figure 2.7 Examples of identified fins at distances from 43 to 162 meters.

Whales at distances greater than 100 meters are identified primarily by observing blows. This is the same method used by Perryman et al. (1999) and is practical to use when the target species and approximate location is already known from other means such as visual observation or hydrophone detection. Figure 2.8 shows 2 sequential frames of whale blows at a distance of 140 meters. Blows are distinguished from whales and background noise by tracking the motion through multiple frames. Blows appear and dissipate quickly while whales show steady movement and background noise (such as sun glare) stays relatively still.

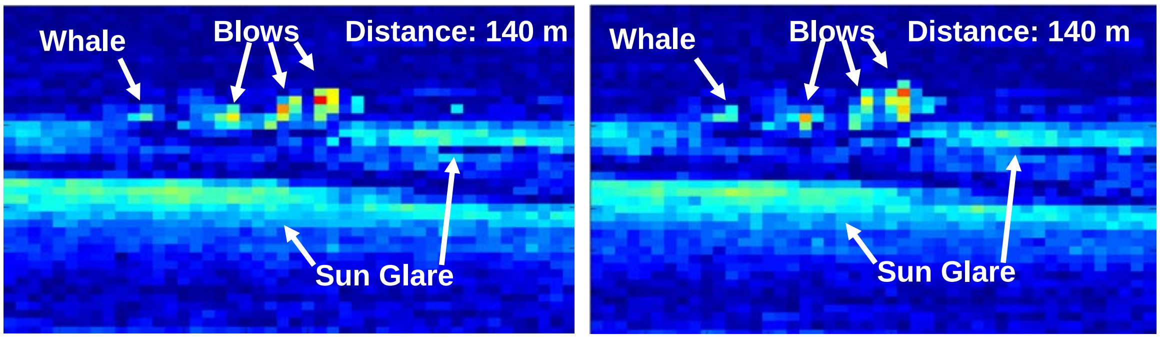

Figure 2.8 Examples of blows detected at 140 meters in two sequential frames.

The smallest blows detected were made up of two pixels at a distance of 162 meters. Although detection is possible with 2 pixels per target (PPT) a higher resolution image is required to distinguish features of the target. The purpose of the monitoring system dictates the required resolution. For example, if a system is being set up to track the population and swimming speed of a known species (such as the study by Perryman et al.), tracking blows with a minimum of 2 pixels per target is sufficient. However, if a study requires an accurate measurement of the whale to sea surface temperature contrast or species identification, more pixels per target are required. Camera and optics selection based on range is discussed in more detail in section 5.1.

In order to obtain an accurate temperature contrast measurement of a target, there must be at least one pixel not biased low by averaging of the target temperature with the lower temperature of the background. The value for each pixel is an average of the radiation received from the area covered by that pixel. Pixels that only partially cover a target (edge pixels) will therefore return a weighted average of the target and the background radiation based on the percentage of the target covered. Recall that whale fins are approximated as a triangle. As shown in Figure 2.9, in order for at least one pixel of a triangle to not be affected by averaging, a minimum of 9 pixels is required.

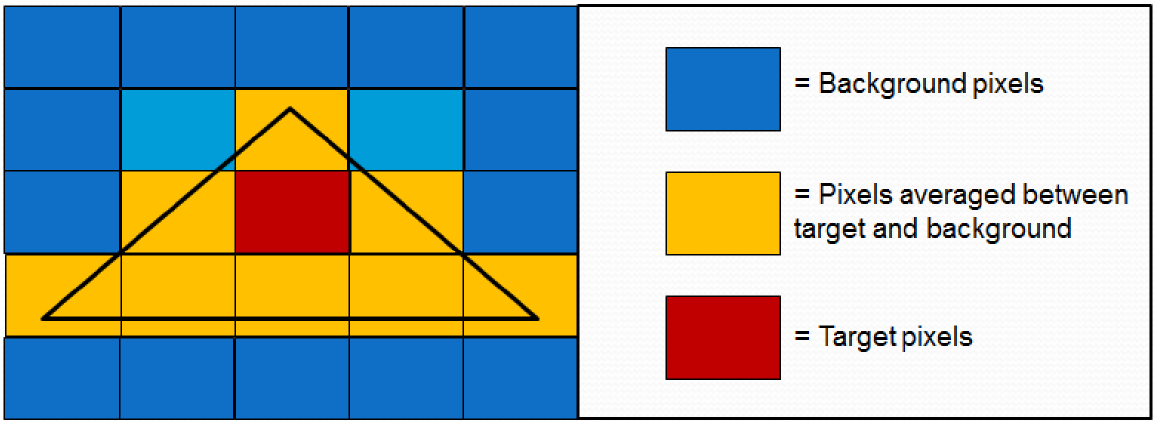

Figure 2.9 An illustration of the minimum number of pixels (9) required for a triangle target in order to have at least one pixel not affected by pixel averaging.

Figure 2.10 shows a killer whale fin observed on July 7th at 19:26 (range 97 m, incidence angle 82°) that exhibits this pattern. The fin is made up of 9 pixels and the center pixel is darker red than any of the other pixels, indicating a higher apparent temperature contrast. Since 8 out of 9 pixels are affected by pixel averaging, the maximum fin temperature contrast is a more accurate estimation of actual temperature contrast than the mean. This applies to any target with a relatively low number of pixels.

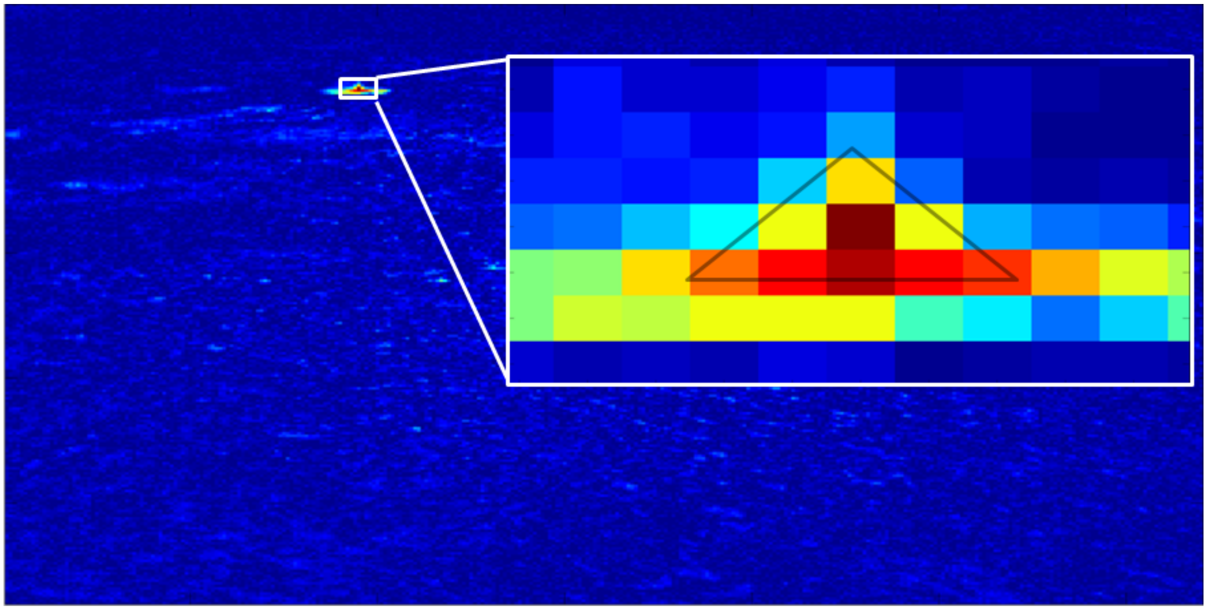

Figure 2.10 Example dorsal fin with 9 pixels from 7/7 at 19:26. It can be seen that the center pixel is darker red (warmer) than the others since it is not affected by pixel averaging.

In summary, the range of a given camera and lens geometry depends on the purpose of the deployment. Two pixels per target (PPT) are adequate for detection; however, at least 9 pixels per target (PPT) are required for accurate temperature contrast measurements.

2.6 Temperature Contrast

The apparent fin to sea temperature contrast measured by an IR camera is expected to be affected by pixel averaging (section 2.5) and incidence angle (section 1.2.3). In this section field measurements are compared with the trends predicted by theory.

2.6.1 Pixel Averaging

As discussed in section 2.5, triangular targets such as killer whale dorsal fins are expected to require a minimum of 9 pixels in order to have at least one pixel unaffected by averaging. Pixels affected by averaging will show a lower apparent temperature contrast since a portion of the pixel area covers the sea surface. Figure 2.11 shows the distribution of maximum fin to sea temperature contrast for all fins. Fins with 9 or more pixels (green) show a higher temperature contrast distribution than fins with fewer than 9 pixels (red).

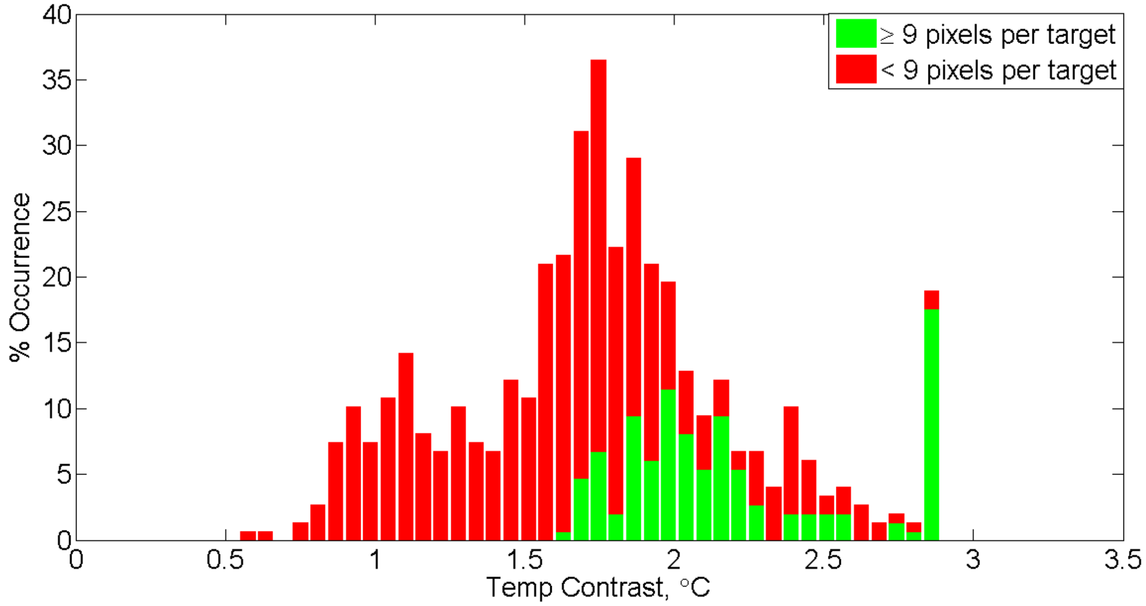

Figure 2.11 Distribution of maximum temperature contrast between dorsal fin bounding triangles and sea surface. Fins with 9 or more pixels are shown in green and fins with less than 9 pixels are shown in red.

For all fins the mean maximum temperature contrast is 1.8 °C. For fins with fewer than 9 pixels the mean is 1.6 °C and for fins with 9 or more pixels the mean is 2.3°C. This confirms that pixel averaging lowers the maximum apparent temperature for fins with less than 9 pixels. Therefore, only fins with 9 or more pixels will be used for the remainder of this analysis.

2.6.2 Incidence Angle

As discussed in section 1.2.3, when viewed at incidence angles above 60°, the apparent temperature of the sea surface is expected to be highly dependent on sky temperature (T_{sky}) because reflected radiation from the sky begins to dominate over emitted radiation from the sea surface. If T_{sky} is less than T_{sea}, the sea surface apparent temperature will decrease with increasing incidence angles. Using infrared images recorded immediately after a non-uniformity correction (NUC), we can determine how much the apparent sea surface temperature changes because of incidence angle. Since the true sea surface temperature is relatively constant, apparent temperature differences in a calibrated image are primarily due to the reflection of the sky temperature. Figure 2.12 shows the same frame as displayed previously in Figure 1.7. The apparent temperature change in the mean image relative to the reference bin is displayed in °C.

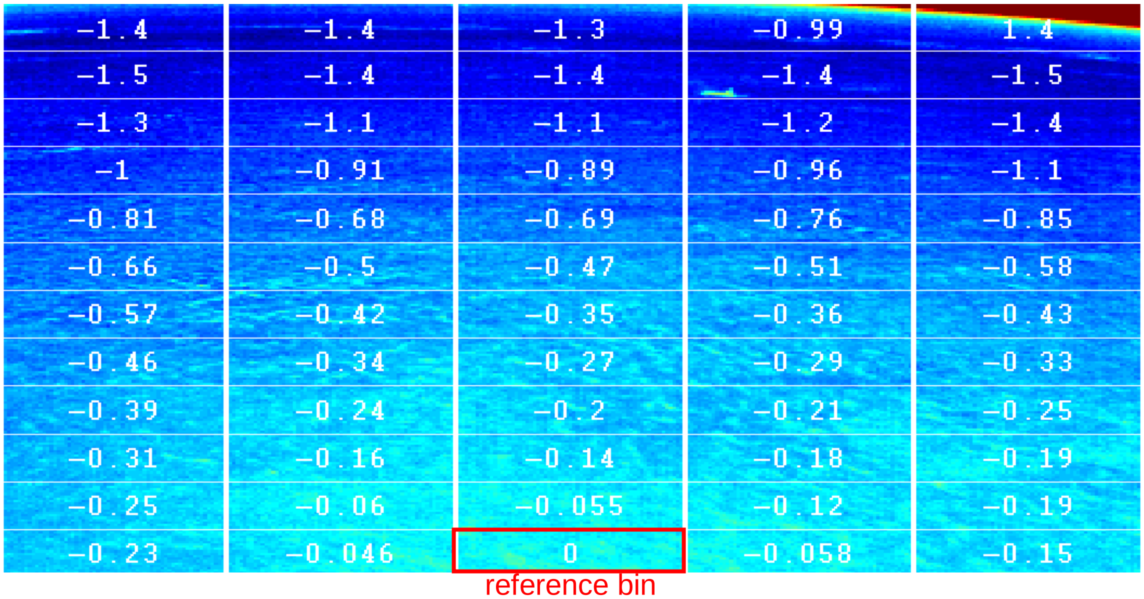

-1.4	-1.4	-1.3	-0.99	1.4
-1.5	-1.4	-1.4	-1.4	-1.5
-1.3	-1.1	-1.1	-1.2	-1.4
-1	-0.91	-0.89	-0.96	-1.1
-0.81	-0.68	-0.69	-0.76	-0.85
-0.66	-0.5	-0.47	-0.51	-0.58
-0.57	-0.42	-0.35	-0.36	-0.43
-0.46	-0.34	-0.27	-0.29	-0.33
-0.39	-0.24	-0.2	-0.21	-0.25
-0.31	-0.16	-0.14	-0.18	-0.19
-0.25	-0.06	-0.055	-0.12	-0.19
-0.23	-0.046	0	-0.058	-0.15

reference bin

Figure 2.12 Sea surface temperature change (°C) relative to the reference bin for the mean image from the 11:45 pass on 7/7. The background image is a single frame from this pass.

These temperatures were calculated by separating the mean image for this pass into 60 bins (sections of 20 x 64 pixels) and calculating the mean apparent temperature of each bin. The mean apparent temperature of the reference bin (the bottom center) was then subtracted from each bin. It can be seen that the apparent sea surface temperature decreases from the bottom to the top of the field of view by as much as 1.5 °C. The top row of bins is slightly warmer than the row directly below it due to the effects of the horizon. Extending this methodology to additional footage, Figure 2.13 shows the apparent temperature change of the sea surface with incidence angle immediately after 3 non-uniformity corrections on July 6th and 3 on July 7th.

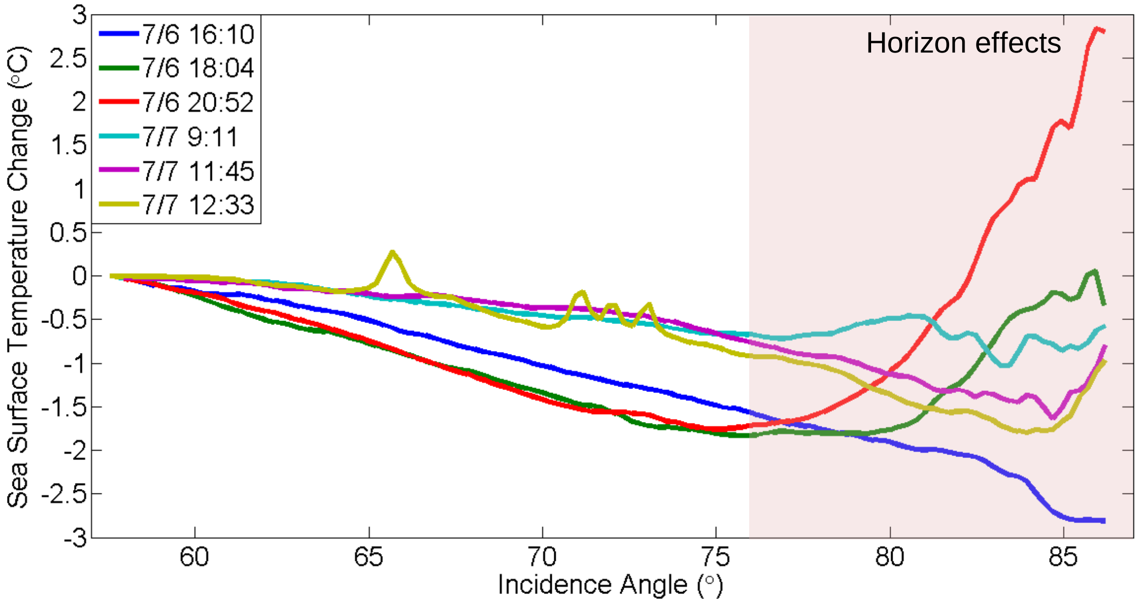

Figure 2.13 Temperature change of the sea surface relative to the reference bin versus incidence angle for the center column of averaged bins (Figure 2.12) for 6 recordings taken immediately after non-uniform correction (NUC).

As expected, a decrease in apparent sea surface temperature with increasing incidence angles can clearly be seen for incidence angles from 58° to 76°. The 4 distinct bumps (66°, 71°, 72°, and 73°) in the 12:33 scene are due to 4 kayakers that passed through the FOV of the camera during this scene, biasing the mean image to a greater extent than the transient from a whale surfacing. The scenes from July 6th show a more negative slope between incidence angle and sea surface temperature, suggesting a colder sky temperature that day relative to the 7th. For incidence angles greater than 76°, the apparent sea surface temperature increases in the 18:04 and 20:52 scenes. This increase is due to glare from the setting sun. The camera faces west and as the sun approaches the horizon more of the sun's radiation is reflected off the sea surface to the camera. Sunset on July 6th was at 21:09 explaining why the glare effect is most pronounced in the 20:52 scene. The mean image from 20:52 is shown in Figure 2.14. The light blue, yellow, and red near the top of the image indicate the increased apparent temperature due to reflection of the setting sun.

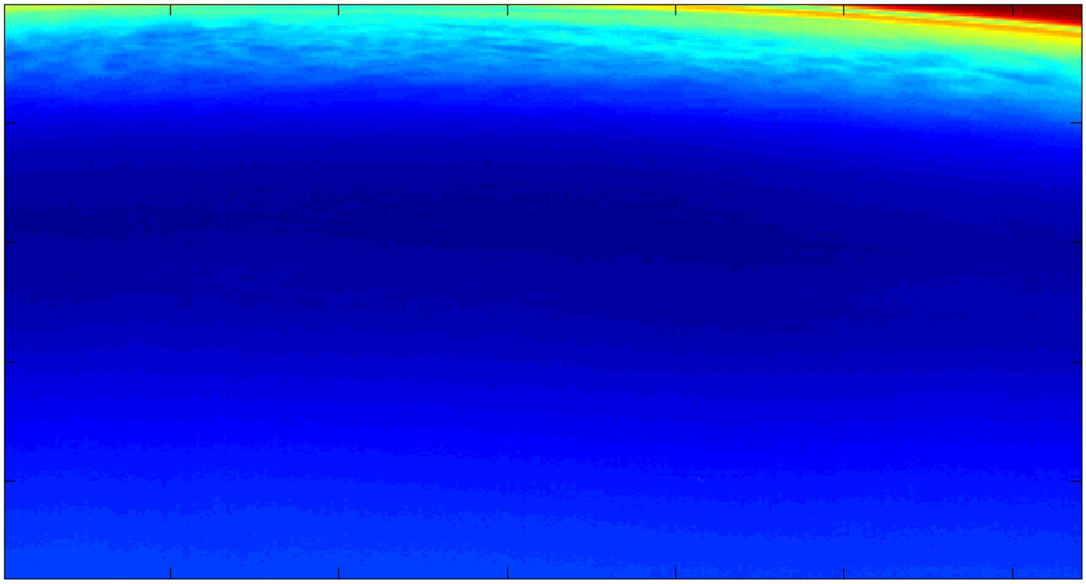

Figure 2.14 The mean image from 7/6 20:52 showing sun glare from setting sun.

To correlate the observed sea surface temperature change with published values of emissivity, Equation 1.14 can be used.

$$\mathrm{M} = \varepsilon_{eff}(\theta_{sea})\mathrm{M}_{sea}(T_{sea}) + \rho_{eff}(\theta_{sea})\mathrm{M}_{sky}(T_{sky}). \qquad 1.14$$

For an arbitrary point *a* equation 1.14 becomes

$$M_a(T_a) = \varepsilon_a \mathrm{M}_{sea}(T_{sea}) + \rho_a \mathrm{M}_{sky,a}(T_{sky,a}), \qquad 2.2$$

where

T_a is the apparent sea surface temperature at arbitrary point *a*,

T_{sea} is the true temperature of the sea surface,

$T_{sky,a}$ is the apparent temperature of the portion of the sky reflected at point *a,*

$\mathrm{M_a}, \mathrm{M}_{sea}$, and $\mathrm{M}_{sky,a}$ are related to $\mathrm{T_a}, \mathrm{T}_{sea}$, and $\mathrm{T}_{sky,a}$ by Planck's law (equation 1.7).

Combining 2.2 with 1.6 and solving for M_{sky} we obtain

$$\mathrm{M}_{sky,a}\left(T_{sky,a}\right) = \frac{M_a(T_a) - \varepsilon_a \mathrm{M}_{sea}(T_{sea})}{(1-\varepsilon_a)}. \qquad 2.3$$

The sea temperature (T_{sea}) is obtained from the NOAA NDBC New Dungeness buoy. For the 11:45 pass on July 7th the reported sea temperature is 10.9 °C (Figure 2.2). Since an external blackbody calibration was not performed on the FLIR A40M during the field observations, the infrared footage indicates accurate temperature changes, but not absolute temperatures. In order to determine the absolute temperature, we relate the change in sea surface temperature shown in Figure 2.12 to the true sea temperature (T_{sea}). Figure 2.15 shows the sea surface emissivity versus the apparent sea surface temperature change (relative to the reference bin) for all the bins shown in Figure 2.12. A least squares fit is used to extrapolate the temperature change from the true sea surface temperature (ε=1) to the reference bin (ε=0.95). It can be seen that the true sea surface temperature (T_{sea}=10.9 °C) is expected to be 0.2 °C warmer than the reference bin, suggesting an estimated reference bin temperature of 10.7 °C.

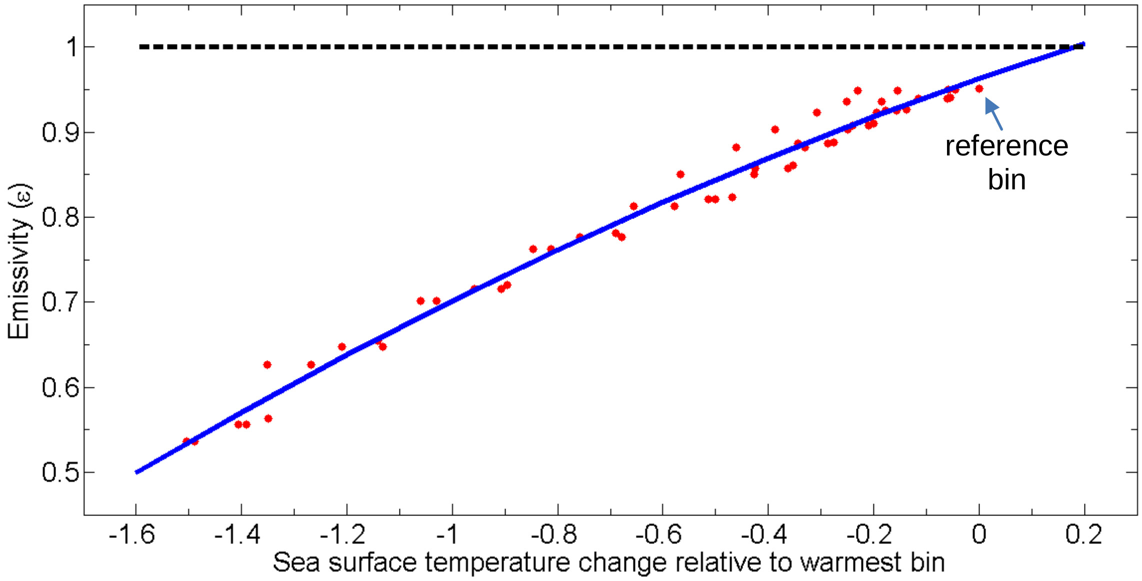

Figure 2.15 Emissivity versus sea surface temperature change in relation to reference bin for all bins shown in Figure 2.12.

Using the estimated reference bin temperature (10.7 °C), the temperature changes from Figure 2.12, and equation 2.3, the estimated sky temperature is calculated for each bin. The resulting sky temperatures are shown in Figure 2.16.

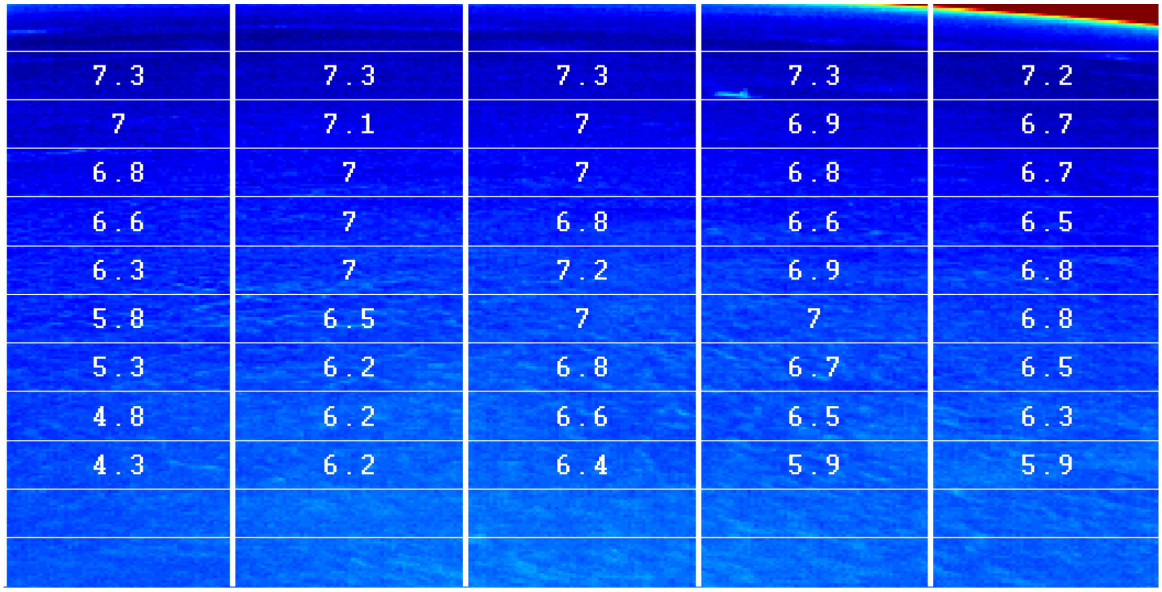

7.3	7.3	7.3	7.3	7.2
7	7.1	7	6.9	6.7
6.8	7	7	6.8	6.7
6.6	7	6.8	6.6	6.5
6.3	7	7.2	6.9	6.8
5.8	6.5	7	7	6.8
5.3	6.2	6.8	6.7	6.5
4.8	6.2	6.6	6.5	6.3
4.3	6.2	6.4	5.9	5.9

Figure 2.16 Estimated sky temperature calculated from apparent sea surface temperature change as shown in Figure 2.12.

The values for the two bottom rows of bins are not included since the emissivity difference from the reference bin is not large enough for an accurate calculation. The values for the top row of bins are not included since they are affected by the horizon. As shown in Figure 2.16, the estimated sky temperature increases with incidence angle. As the incidence angle increases, so does the reflected zenith angle (θ_z). At high zenith angles, the optical path through the atmosphere is longer than for zenith angles near zero (directly upward). This path length can be expressed in atmospheric masses (m_a), where $m_a = 1$ is equal to the path length through the atmosphere at the zenith (θ_z). Figure 2.17 shows the relationship between incidence angle, zenith angle, and air mass. Since the atmosphere radiates relative to the ambient temperature, the apparent sky temperature will increase with increasing atmospheric mass and the results shown in Figure 2.16 are physically justified.

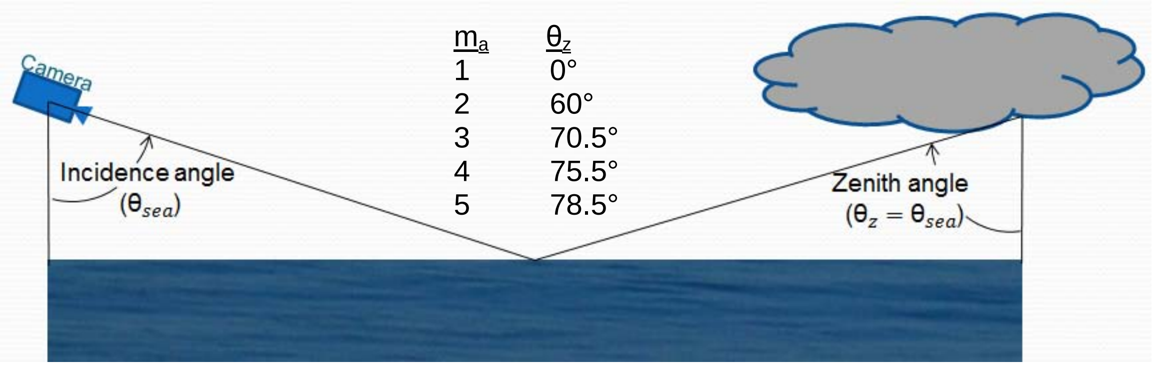

Figure 2.17 The relationship between incidence angle, zenith angle, and air mass.

We can use the estimate of T_{sky} to predict the change in fin to sea surface temperature contrast with incidence angle. As discussed in section 1.2.3, the incidence angle to a whale's dorsal fin (θ_{fin}) is small relative to the incidence angle to the sea surface. Therefore, the apparent temperature of the fin will stay relatively constant. At large incidence angles the apparent temperature of the sea surface decreases so the fin to sea surface contrast is expected to increase. Figure 2.18 shows both the observed and expected temperature contrasts as a function of incidence angle.

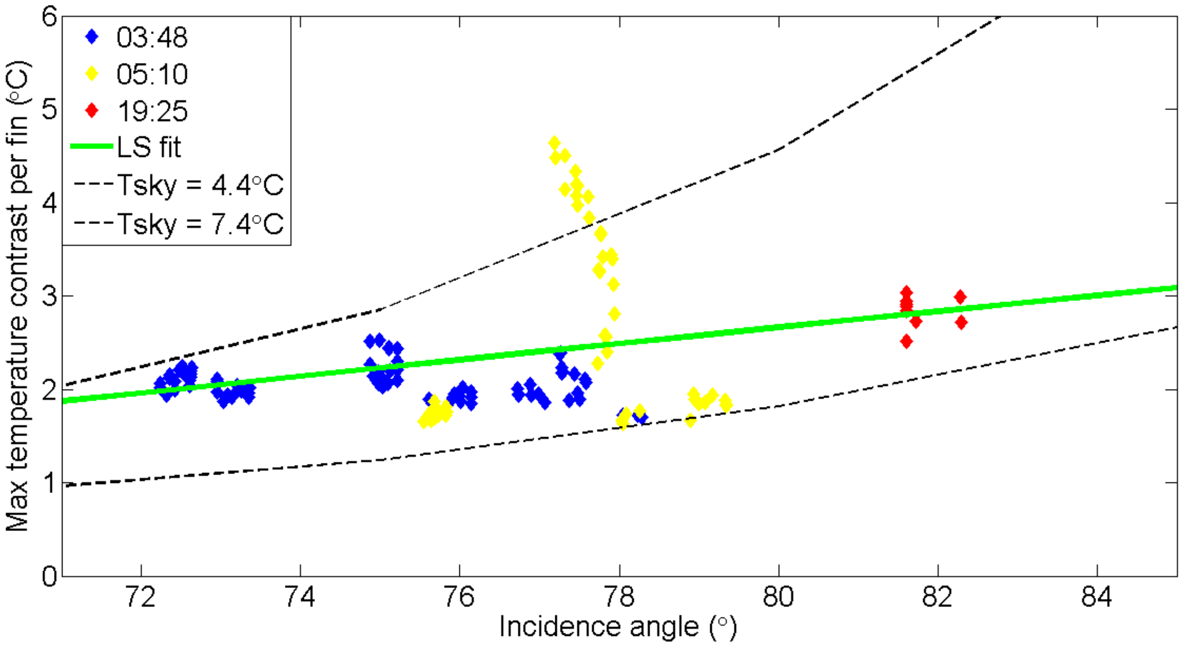

Figure 2.18 Observed and predicted fin to sea temperature contrast as a function of incidence angle. Predicted values were calculated from the minimum and maximum estimated sky temperatures (Figure 2.16). Only fins with 9 or more pixels are included (Section 2.6.1).

The predicted fin to sea temperature contrasts (dashed lines) were calculated using equation 1.14 and the minimum (4.4 °C) and maximum (7.4 °C) estimated sky temperatures from Figure 2.16. Observed maximum fin to sea temperature contrasts for fins with 9 or more pixels are shown. For fins with less than 9 pixels (frequently the case at larger incidence angles), pixel averaging causes an artificial decrease in the observed temperature contrast as discussed in section 2.6.1. To obtain the best fit of the observed temperature contrasts, the predicted temperature contrast curves (dashed lines) were adjusted with an empirical offset of 0.4 °C at an incidence angle of 0°. As can be seen, the majority of observed values fall within the predicted envelop at a given incidence angle. The slope of the least squares fit (LSF) curve (green line) is less steep than the predicted slope for both the minimum and maximum sky temperature. The coefficient of determination (R^2) for the LSF is only 0.18 indicating that there is not a strong trend in the data.

The fins from the pass at 5:10 have a wide range of observed temperature contrasts, some falling outside the range of values predicted by theory. The standard deviation of temperature contrasts for this pass is 1 °C, nearly an order of magnitude higher than the other two passes (0.17 and 0.15 °C). Although the reasons for this variability are unknown, one possible cause could be reflection of the horizon on the whales' fins. The 5:10 pass is the only footage collected of whales during the hours of twilight. On July 7th, civil dawn began at 4:40 and sunrise was at 5:20. During the 5:10 pass, the east horizon (directly behind the camera) was illuminated. It is possible that the variability of whale fin temperature contrast is due to reflection of the horizon on the whale fins, but future study is required to test this hypothesis.

2.7 Discussion

The apparent temperature contrast between a killer whale dorsal fin and the surround sea surface is a combination of the true temperature contrast and the effects of emissivity. The true temperature contrast is unknown and is expected to vary from fin to fin. Kastings et al. (1989) measured the fin to sea temperature contrast of three captive killer whales using a skin-surface thermistor and found that it ranged between 1.4 and 2.2 °C. Since a thermistor was used, these values represent the temperature contrast from the skin-surface of the dorsal fin. When a whale surfaces, the dorsal fin remains covered with a thin film of sea water. Since water is virtually opaque to infrared radiation the fin temperature measured by an infrared imager is the temperature of the water on the surface of the fin, and is therefore expected to be lower than the fin skin surface temperature. Cuyler et al. (1992) measured the fin to sea temperature contrast of free living minke, humpback, and fin whales using an infrared imager and found that it ranged between 0.5 and 1.9 °C.

As discussed in section 2.6.2, the predicted fin to sea temperature contrast curves fit the observed data best with an empirical offset of 0.4 °C at an incidence angle 0°. This suggests a true fin to sea temperature contrast of 0.4 °C, however there is not a strong enough trend in the observed data ($R^2 = 0.18$) for this estimate to be statistically significant. Also, the slope of the least squares fit curve in Figure 2.18 is less than the predicted trend suggesting a true temperature contrast greater than 0.4 °C. In addition, the apparent temperature of the sea surface varies by as much as 1.5 °C (Figure 2.12) due to emissivity effects, and the mean observed temperature contrast of fins with 9 or more pixels is only 2.3 °C (Figure 2.11). Although an accurate estimate of the true fin to sea temperature contrast is not possible with the current data, it can be inferred that emissivity effects make up a significant portion of the observed fin to sea temperature contrast.

Chapter 3 - Automated Detection

Infrared imagery of marine mammals offers the added benefit of simplifying automated detection. Automated detection using visual imagery relies principally on detected motion. Since the sea surface is in constant motion, this can lead to many false detections. Automated detection using infrared imagery is based on thermal gradients. Since the temperature of the sea surface is nearly uniform in calm conditions, there are fewer false detections. However, in rough seas, the incidence angles to surface waves can give rise to elevated apparent temperature and increasing infrared “clutter”. Basic detection systems for both visual and infrared imagery were tested at Lime Kiln Park. The standard motion detection provided with the Canon VB-C50FSi showed constant detection due to tidal currents and surface waves. By adjusting the sensitivity and creating a mask for waves in the near field of view, the detections could be limited to once every few minutes, however, with these settings, passing whales were also not detected.

Infrared footage was processed through two phases of automated detection. First, footage was analyzed using the default object recognition functions in MATLAB’s image processing toolbox. Not surprisingly, objects (waves, surface disturbances, boats, birds, etc) were detected in nearly every frame. Next, a simple algorithm was written to help distinguish whales from false detections. Thresholds were applied to classify objects as whales based on signal intensity, total area, perimeter, and eccentricity. In addition, neighboring frames are compared to filter false detections in singular frames. A flowchart of the developed algorithm is shown in Figure 3.1 including the MATLAB functions used in parentheses.

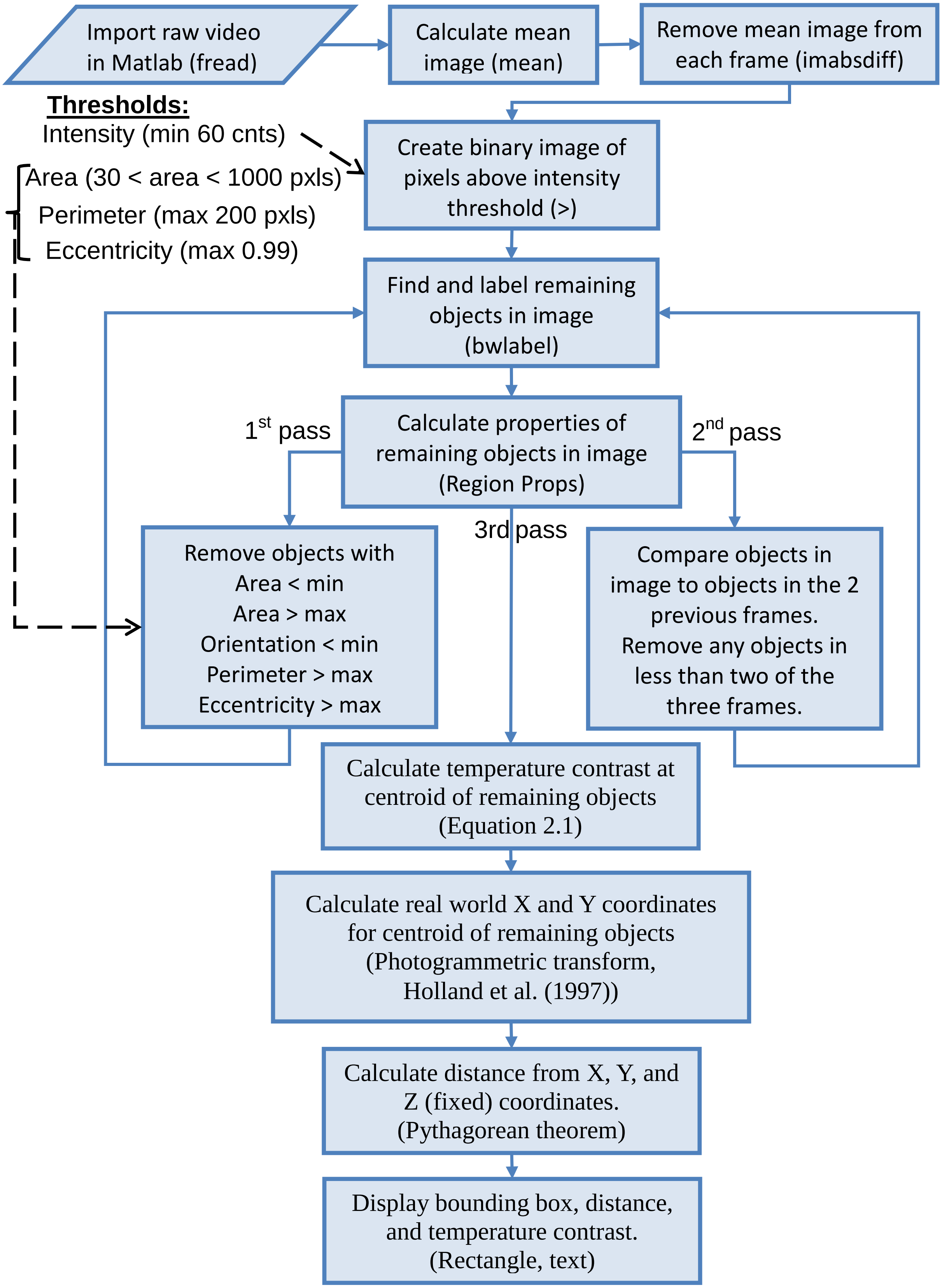

Figure 3.1 Flow chart showing logic of automated detection program implemented in MATLAB.

The thresholds shown in Figure 3.1 were determined empirically through trial and error. Using estimated threshold values, the footage from the July 7th pass at 3:48 (longest pass) was analyzed with the automated detection algorithm and false detections were systematically removed by modifying the threshold values. The intensity threshold (60 counts) corresponds to a minimum temperature contrast of 0.6 °C (equation 2.1). The area minimum (30 pixels) and maximum (1000 pixels) will vary greatly depending on the distance to the target. The current algorithm is therefore only applicable to surfacing events between 40 and 60 meters (the range of surfacing events from the 3:48 pass). The area threshold removes false detections from very small and very large surface disturbances. Detected surface waves with areas larger than the minimum area threshold frequently appear as long arcs which have large perimeters and eccentricities but small enough areas to be below the maximum area threshold. For these false detections the perimeter (max 200 pixels) and eccentricity (max 0.99) thresholds were added. Objects passing all criteria are identified with a bounding box and range and temperature contrast are displayed. Figure 3.2 shows an example of the output of the developed algorithm and Table 3.1 summarizes the results of the developed algorithm on the July 7th pass at 3:48.

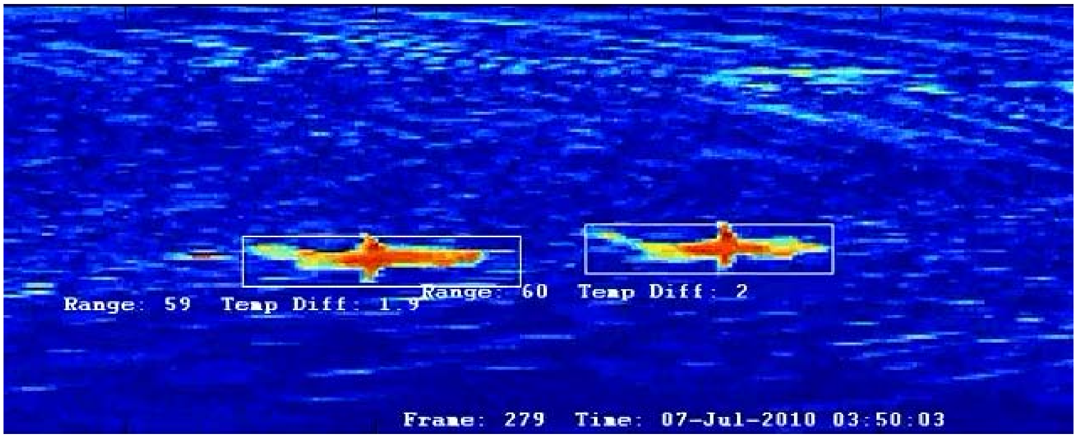

Figure 3.2 Output of the automated detection algorithm. Whales are distinguished from background variations and highlighted with a bounding rectangle. Range and temperature contrast are also displayed.

Table 3.1 Results of the automated detection algorithm on the July 7th pass at 3:48.

	Duration	Frames	Whales	False detections
Original	150 seconds	1130	71	-
Simple Algorithm	9 seconds	70	60	42
Percent	6%	6%	85%	-

The algorithm shows detection in only 70 frames (6% of the original footage) and accounts for 85% of the surfacing whales identified by manual review. This shows that even a simple algorithm can significantly reduce the footage requiring manual review. With the proper resources, a more sophisticated algorithm could be developed to increase the percentage of whales identified and decrease the false detections. The addition of video tracking, such as that used in computer vision, would allow identified objects to be tracked through multiple frames. Tracking systems first predict the location of an object being tracked in the next frame and then identify the object (Trucco & Plakas, 2006). By tracking whales through multiple frames it is conceivable that an automated detection program could be developed to mimic the shape and motion recognition of the human eye and either eliminate or significantly decrease the amount of footage requiring manual review.

Chapter 4 - Benefits of Infrared Imagery

In this chapter, the benefits of infrared imagery over visual observation are quantified for use in observing a tidal energy pilot project in northern Admiralty Inlet. Performance data for infrared imagery is not available for all weather conditions because of the limited literature regarding infrared detection of marine mammals (as summarized in Section 1.4). The field observations described in Chapter 2 were recorded in ideal weather conditions (clear skies, calms seas, and wind speeds below 4 m/s) and cannot provide additional insight. Therefore, it is not possible to construct a full performance gradient model for marine mammal detectability based on meteorological data. After reviewing the underlying physics behind infrared and visual camera performance, pass-fail criteria for detectability are established. These criteria are based on relevant literature from the fields of infrared detection of ground targets, free space optics (FSO), and Civil Aviation. These criteria are then compared to weather conditions at Admiralty Inlet for each hour over the course of a year (2008 is used as a representative year based on availability of data). Although the meteorological data used is specific to Admiralty Inlet, the methodology can be transferred to any location. The parameters considered are summarized in Table 4.1.

Table 4.1 Parameters considered and the expected effects on detectability.

Parameters	**Effects**	
	Visual	**Infrared**
Ambient Light	Excludes night observation	No effect
Relative Humidity	Partial signal attenuation	Partial signal attenuation
Fog	Heavy signal attenuation	Heavy signal attenuation
Sea State	Introduces background noise masking targets	Introduces background noise masking targets

Meteorological data is compiled from three sources, the Whidbey Island AgWeatherNet Station maintained by WSU, the Whidbey Island Naval Air Station (NAS), and NOAA's Nation Data Bouy Center station 46088 (New Dungeness, WA). Table 4.2 shows the data used from each station and Figure 4.1 shows the location of the weather stations relative to the proposed tidal energy site at Admiralty Inlet. The most recent year of complete data from the Whidbey Island NAS is 2008, which is adopted as the reference year. Hourly ratings from the Whidbey Island AgWeatherNet Station are used as a baseline and correlated to the closest available readings from the Whidbey Island NAS and the NDBC buoy.

Table 4.2 Weather data used for comparison between IR and traditional observations.

Weather Station	Data Acquired through	Latitude	Longitude	Elevation (m)	Data used
AgWeatherNet Whidbey Island Station	WSU AWN website	48.2 N	122.7 W	79	Air Temp, Relative Humidity
Whidbey Island NAS WBAN # 24255	NOAA, NCDC	48.35 N	122.65 W	14	Visibility
NDBC Station 46088 New Dungeness, WA	NOAA, NDBC	48.333N	123.167 W	4	Significant wave height

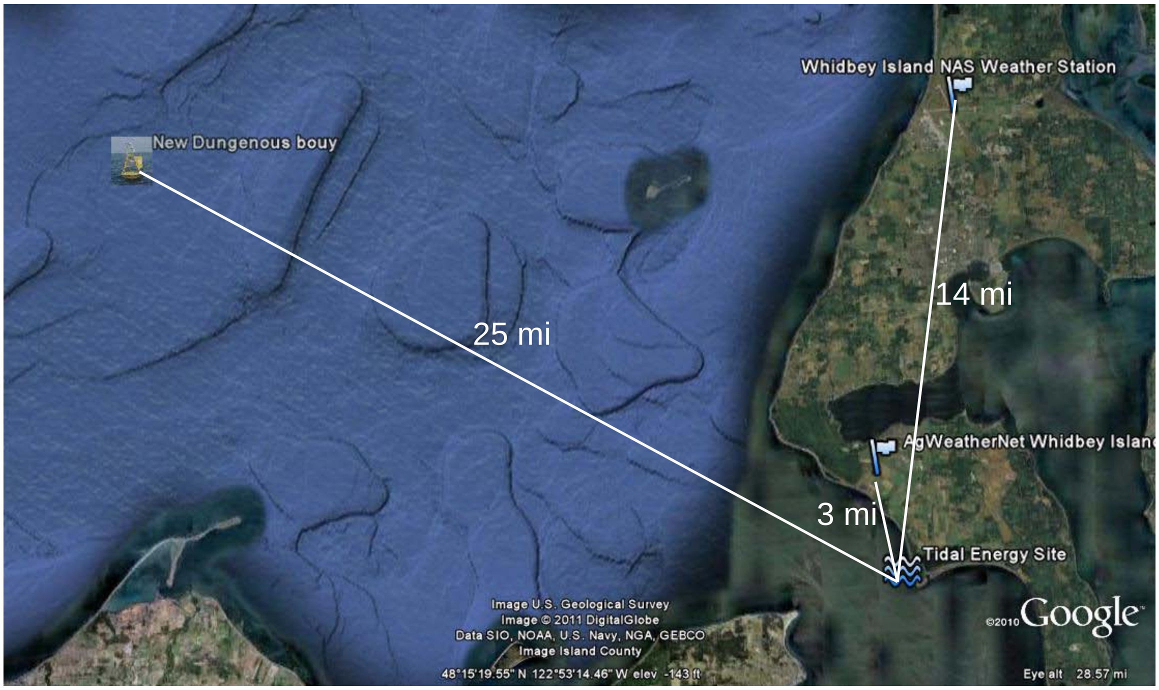

Figure 4.1 Location of weather stations compared to the proposed tidal energy site in Admiralty Inlet

4.1 Ambient Light

A traditional digital camera records the visible light reflected off target surfaces and therefore requires a source of ambient light. The amount of ambient light required for reliable detection will vary depending on the camera used. The Canon VB-C50FSi used for this study has a minimum illumination rating of 1 lux (1 lumen/m^2).

The level of outdoor ambient light varies in a daily periodical cycle based on the rotation of the earth. Twilight is the period before sunrise and after sunset where visible light from the sun is reflected by the upper atmosphere. Dawn is the beginning of morning twilight and dusk is the end of evening twilight. Twilight can be separated into civil twilight, nautical twilight, and astronomical twilight. Civil twilight is the period before sunrise or after sunset when the center of the sun is between 0 and 6° below the horizon. With good climatic conditions there is enough ambient light to clearly distinguish terrestrial objects during civil twilight without an artificial light source (U.S. Naval Observatory, 2011). At 48° N latitude (latitude of Admiralty Inlet) civil twilight varies between 30 and 41 minutes in duration depending on the season.

Nautical twilight is the period when the sun is between 6° and 12° below the horizon. The end of nautical twilight is when (under good climatic conditions) the horizon is no longer distinguishable for sea navigation. At 48° N latitude nautical twilight varies between 35 and 57 minutes in duration depending on the season. Astronomical twilight is the period when the sun is between 12° and 18° below the horizon. During astronomical twilight, the illumination from the upper atmosphere is so faint it is nearly imperceptible. Distinction between the hours of astronomical twilight and night is only applicable to astronomical observations of faint celestial bodies (U.S. Naval Observatory, 2011).

Footage was reviewed to qualitatively evaluate ambient light from observations at both Lime Kiln Park (July, 2010) and Admiralty Inlet (December, 2010). There appears to be sufficient light for marine mammal detection at sunrise, sunset, civil dawn (the beginning of civil twilight), and civil dusk (the end of civil twilight). As shown in Figure 4.2 and Figure 4.3, by nautical dusk there is no longer enough ambient light for detection.

Figure 4.2 **Images from the Canon VB-C50FSi camera at Lime Kiln Park on 7/8/2010 showing available ambient light during twilight. a) Image at sunset (21:08 PDT), b) Image at civil dusk (21:47 PDT), c) Image at nautical dusk (22:41 PDT).**

Figure 4.3 **Images from the Canon VB-C50FSi camera at Admiralty Inlet on 12/21/2010 showing available ambient light during twilight. a) Image at sunset (16:20 PST), b) Image at civil dusk (16:56 PST), c) Image at nautical dusk (17:36 PST).**

The transition from a usable image to one that is too dark for detection takes place during nautical twilight. As a conservative estimate, the hours between civil dawn and dusk are considered the usable hours for a digital video camera for marine mammal detection. For 2008 numbers, the hours between civil dawn and dusk make up 56% of the year (U.S. Naval Observatory, 2011).

4.2 Atmospheric Conditions

Attenuation is the reduction of electromagnetic radiation intensity as it propagates through a medium (e.g. air). The transmissivity of a medium is the fraction of electromagnetic radiation transmitted and is a measure of attenuation. The transmissivity of air (i.e. the atmosphere) varies with changing conditions. The radiation received at a distance (d) from the target is related to the initial radiation of the target by the Beer-Lambert law

$$\tau(\lambda, d) = \frac{M_r(\lambda)}{M_0(\lambda)} = e^{-\gamma(\lambda)d} \qquad 4.1$$

where

$\tau(\lambda, d)$ is the spectral transmissivity of the atmosphere through distance d,

$M_r(\lambda)$ is the radiation received at distance d from the target,

$M_0(\lambda)$ is the initial radiation emitted or reflected by the target,

$\gamma(\lambda)$ is the total attenuation (or extinction) coefficient per unit length.

The attenuation coefficient is composed of terms representing the primary mechanisms that lead to signal attenuation; absorption and scattering (Naboulsi, Sizen, & Fornel, 2004).

$$\gamma(\lambda) = \alpha_m(\lambda) + \beta_a(\lambda) \qquad 4.2$$

where

$\alpha_m(\lambda)$ is the absorption coefficient

$\beta_a(\lambda)$ is the scattering coefficient

4.2.1 Absorption

Absorption occurs when a portion of the electromagnetic radiation from the source is absorbed by molecules in its path. The most abundant atmospheric gases are nitrogen, oxygen, water vapor, carbon dioxide, methane, nitrous oxide, carbon monoxide, and ozone. Out of these, water vapor and carbon dioxide are, by far, the most important absorbing molecules (Kruse, McGlauchlin, & McQuistand, 1962).

The band absorption of water vapor and carbon dioxide is what creates the spectral pattern of atmospheric transmittance shown in Figure 4.4. Carbon dioxide is fairly evenly distributed throughout the atmosphere, varying from 0.03% - 0.04%. Water vapor, on the other hand, can vary greatly from 0.01% - 1% depending on location, temperature, and relative humidity (Kruse, McGlauchlin, & McQuistand, 1962).

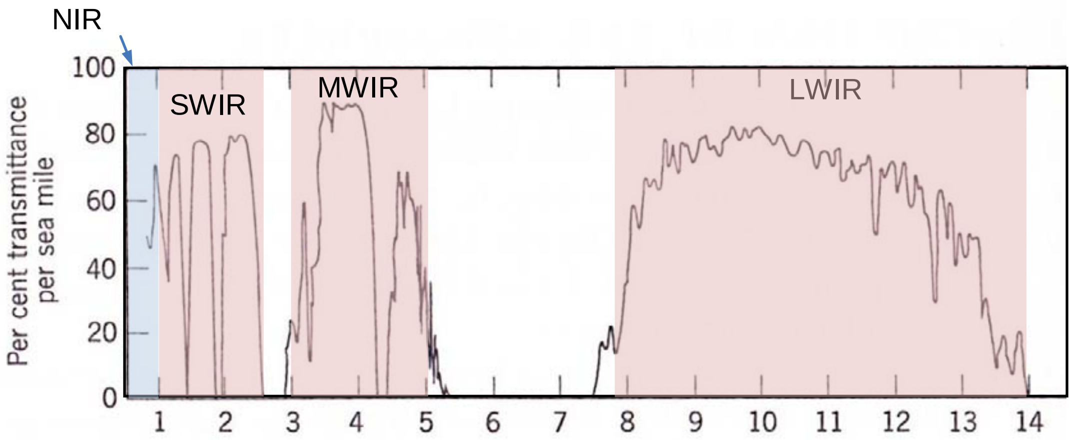

Figure 4.4 Atmospheric transmittance due to absorption primarily from water vapor and carbon dioxide (Kruse, McGlauchlin, & McQuistand, 1962).

Infrared imagers are designed to operate within the atmospheric windows of greatest transmissivity (MWIR, 3-5 µm, and LWIR, 8-14 µm). As shown in Figure 4.4, within these windows, transmissivities range up to 80% per sea mile suggesting that signal attenuation due to molecular absorption will be negligible for the distances dealt with in this study (1 km). The transmissivity tables compiled by Stull et al. (1964) and Wyatt et al. (1964) are used to test this expectation.

The first step is to calculate the mass of each of the absorbing species within the path between the target emitter and the receiving instrument. The total amount of CO_2 varies with distance, temperature, and pressure. The tables provided by Stull et al (1964) give the transmissivity based on the wave-number (cm^{-1}) and the amount of CO_2 in atm-cm. NOAA’s most recent report of carbon dioxide in the atmosphere shows a concentration of 389.69 ppm (Tans, 2010). In order to calculate the amount of CO_2 in the radiation path we use the following equation

$$QntyCO_2 = d * P * 389.69 * \frac{273}{T} * 10^{-4} \qquad 4.3$$

where

d is the distance in meters,

P is the atmospheric pressure in atmospheres,

T is the air temperature in Kelvin (Wayne, 1991).

The amount of H_2O will vary with the relative humidity, air temperature, and distance.

$$QntyH_2O = d * S_{mm} * RH * 2.88651 * \frac{10^{-2}}{T} \qquad 4.4$$

where

S_{mm} is the saturated water vapor pressure in mm of mercury,

RH is relative humidity (Wayne, 1991).

Using equations 4.3 and 4.4, the amount of CO_2 and H_2O in a 1 km path is calculated for each hour of 2008. The corresponding transmissivities for CO_2 (τ_{CO2}) and H_2O (τ_{H20}) are then obtained from tables (Stull et al., 1964; Wyatt et al., 1964). The transmissivities are tabulated by wave number in increments of 50 cm^{-1}. To estimate the transmissivity for the LWIR band (7.5-14 µm), the average is taken of the individual transmissivities for wave numbers 550-1350 cm^{-1}. The total transmissivity is the product of the CO_2 transmissivity and the H_2O transmissivity;

$$\tau_{total} = \tau_{CO_2} * \tau_{H_{2}O}. \qquad 4.5$$

The calculated transmissivities ranged from 59% to 83%. A transmissivity of 59% would degrade a source with a true temperature contrast of 2.3 °C (average observed) to approximately 2 °C, which is still easily detectable. This verifies that signal attenuation due to absorption of CO_2 and H_2O molecules is unlikely to interfere with detection at these distances (1 km). This is in agreement with the literature. For example, Dhar and Khan (2008) reported a recognition range of 10 km for a 2.3 x 2.3 meter target with a 1.25 °C temperature contrast in 90% relative humidity and an ambient temperature of 20 °C.

4.2.2 Scattering

Particles suspended in the air (aerosols) scatter electromagnetic radiation away from the receiving sensor. Scattering occurs when particle radii are of the same order of magnitude as the wavelength (Naboulsi, Sizen, & Fornel, 2004). Therefore, smaller particles (radii 0.1-1 µm) have a greater effect on short wavelength radiation (visible spectrum) while larger particles (radii > 1 µm) have a greater effect on the IR spectrum. Aerosols consist of dust, carbon, smoke, water droplets, salt, or even small living organisms (Kruse, McGlauchlin, & McQuistand, 1962).

Scattering occurs most predominantly in foggy conditions. Fog is a collection of visible particles that are made up of aerosol nuclei and condensed water. In high humidity conditions water condenses to increase the size of the suspended particles. The radii of typical aerosols vary from 0.0001 - 1 µm but can grow up to 30 µm in fog (Beier & Gemperlein, 2004). The severity of fog is classified using the standard international civil aviation organization (ICAO) categories shown in Table 4.3. The

ICAO categories are based on the runway visual range (RVR or, simply, visibility) which is defined as the distance where image contrast is degraded by 98%.

To calculate the atmospheric transmissivity for different conditions and wavelengths, a computer programed called MODTRAN (Moderate Resolution Propagation Model) has been developed by the US Air Force Research Laboratory. MODTRAN uses a narrow band model that takes into account six climate categories and six aerosol categories (Beier & Gemperlein, 2004). Using MODTRAN, Beier & Gemperlein (2004) modeled the attenuation of visible and IR radiation due to fog. Table 4.3 summarizes the minimum and maximum visibility for each ICAO category and the range used in the MODTRAN modeling of Beier and Gemperlein (2004). They further separate CAT III fog into IIIa and IIIc, however this distinction is not necessary for this study since both IR and visible cameras would be ineffective for this application in fog more intense than CAT III.

Table 4.3 ICAO fog categories used for classification of visibility data from Whidbey Island NAS as well as the range used in the MODTRAN modeling by Beier and Gemperlein (2004).

Category	RVR (m)	RVR used by Beier & Gemperlein (2004) (m)
CAT I	732 – 1981	1220
CAT II	366 - 732	610
CAT III	0 - 366	IIIa 305 IIIc 92

As shown in Table 4.3 the maximum visible range for CAT II fog is only 732 meters. Since the proposed tidal energy site is 1000 m from the shore, visible detection would not be possible in CAT II fog. For CAT I fog the visible range is 732 – 1981 meters so a visible camera will work in light CAT I fog but not in heavy CAT I fog. Therefore, as a conservative estimate for comparing the effectiveness of infrared and visual cameras, it is assumed that a visible detection is possible in fog of CAT I or less.

Beier and Gemperlein conclude that both IR windows (MWIR 3-5 µm and LWIR 8-12 µm) show significantly better detection ranges than visible in CAT I fog. This holds true of all climatic zones, seasons, and types of aerosols included in the MODTRAN code. In CAT II fog, only the LWIR window (8-12 µm) shows range improvement over the visible spectrum. For CAT III fog there is no improvement over the visual range by using IR cameras (Beier & Gemperlein, 2004).

Figure 4.5 shows the apparent temperature contrast versus distance for CAT II fog as estimated by Beier & Gemperlein. As highlighted in red, a 2 x 2 meter target with an initial temperature contrast of 1 °C is expected to show an apparent temperature contrast of only 0.04 °C at a distance of 1 km.

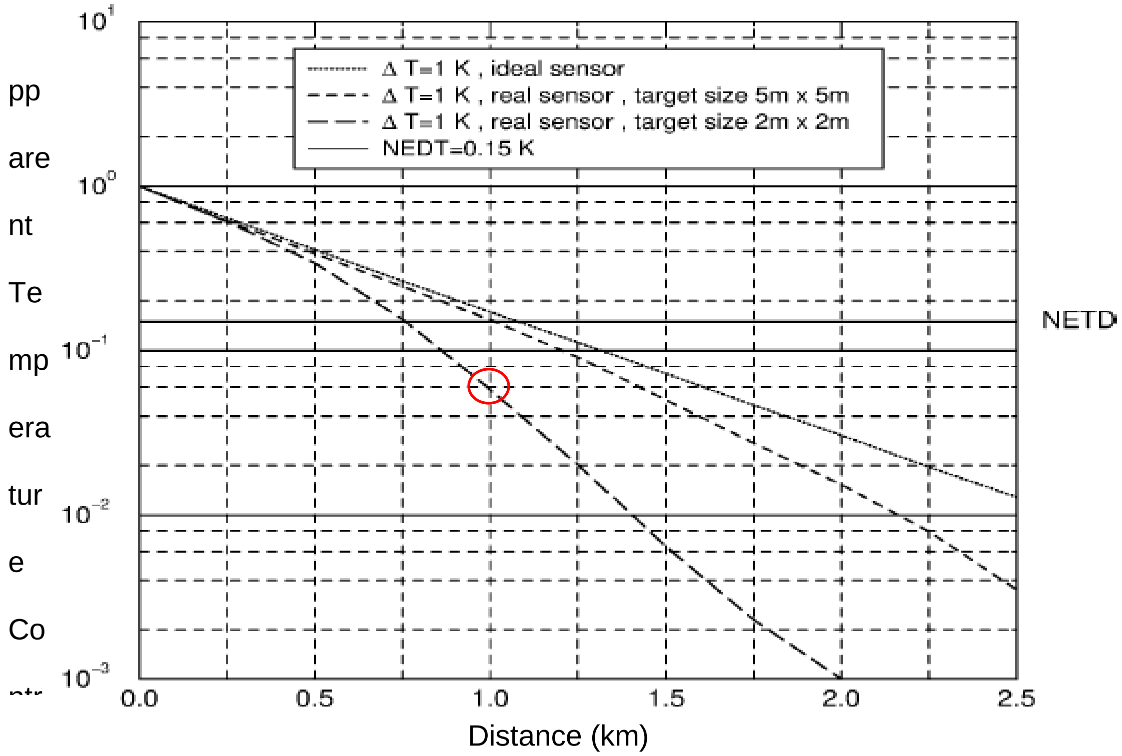

Figure 4.5 Apparent temperature contrast versus distance for real and ideal LWIR sensors (8–12 μm) in CAT II fog (visual range 610 m). Model generated using MODTRAN with the midlatitude winter climate model (background temp = 272.2 K) and radiative fog. (Beier & Gemperlein, 2004).

For killer whale detection, the initial temperature contrast is higher (2.3 °C, section 2.6). However, the target is smaller (approximately 1 m x 1m). Beier and Gemperlein note that due to the larger average radii of maritime aerosols they always result in the lowest detection range for a particular fog class. Figure 4.5 is based on radiative fog, so it is reasonable to assume that the signal attenuation over 1 km would be greater for maritime aerosols. Although detection with an IR camera may be possible in very light CAT II fog, detection would be difficult and so the same criteria for the effectiveness of IR observation are used as for visual (i.e. infrared detection is possible in fog of CAT I or less).

To assess the effectiveness of IR or visual observation at the proposed tidal energy project, hourly visibility readings are obtained from the Whidbey Island Naval Air Station. As shown in Figure 4.6, the visibility is rated at 16 km (highest reported value) 71% of the time. In other words, visibility is often excellent at this location.

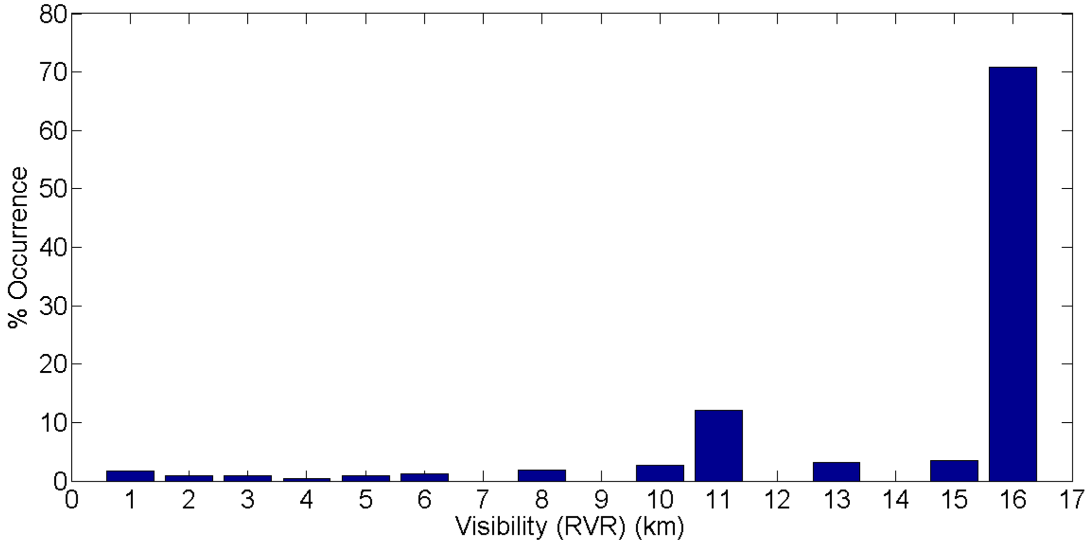

Figure 4.6 Visibility distribution by km from Whidbey Island NAS for the full year 2008.

Using the ranges given in Table 4.3, the visibility ratings from the Whidbey Island NAS (Figure 4.6) are separated into CAT I, II, and III fog. As shown in Figure 4.7, CAT I makes up the highest percentage at 1.2%. From this alone we can conclude that attenuation due to fog will not be a significant consideration for detection and monitoring at Admiralty Inlet. When the criteria for detection in more severe fog are applied, hours of possible detection are decreased by 1%.

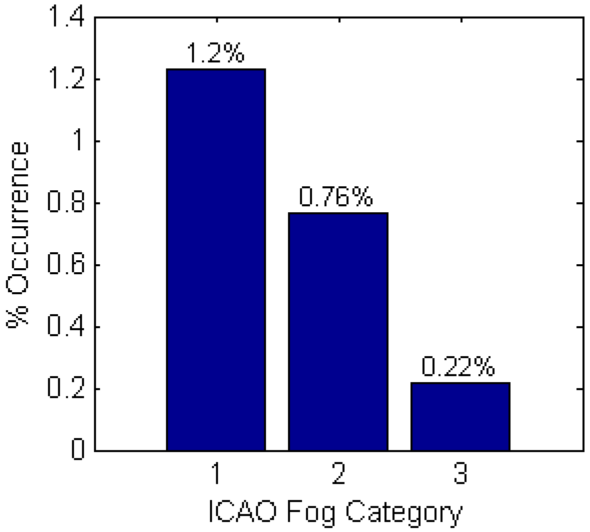

Figure 4.7 Distribution of fog by ICAO category at Whidbey Island NAS for 2008.

4.3 Sea State

High sea states can severely impact detection because of increased “clutter”, both visual and infrared. As shown in Figure 1.10, the emissivity of a whale fin protruding normal to the sea surface is greater than the emissivity of the sea for large incidence angles. This same emissivity effect makes surface waves appear warmer than the surrounding water. High waves can also mask the target by obscuring the visual path and creating mist from white caps. In their field observations using IR binoculars, Baldacci et al. (2005) conclude that for sea states higher than “2” or “3”, detection is no longer reliable for either visual or IR (Baldacci, Carron, & Portunato, 2005). We will interpret this to mean detection is possible for sea states of 2 or lower.

To evaluate the effect of sea state on observations in Admiralty Inlet, significant wave height data from the New Dungeness buoy are used. As shown in

Figure 4.1, this buoy is located 25 miles from the proposed tidal energy site. Although this is in relatively close proximity to the site, the buoy is located in much deeper water in the Strait of Juan de Fuca, and is more exposed to Pacific swell. Figure 4.8 shows the distribution of significant wave height data from the NOAA NDBC New Dungeness buoy. The significant wave height at this buoy is likely to overstate the actual surface conditions in Admiralty Inlet.

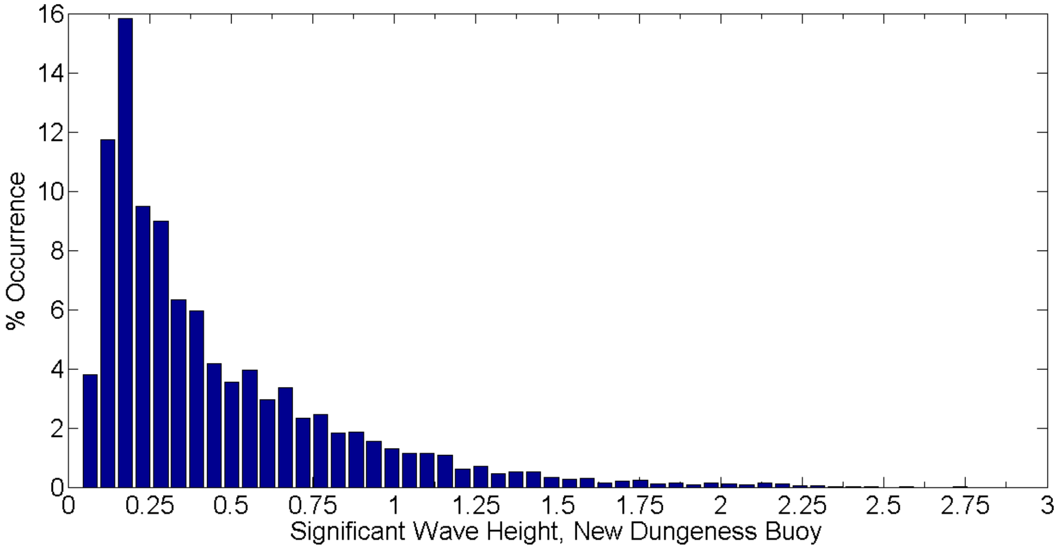

Figure 4.8 Significant Wave Height Distribution for the full year 2008. Data from NOAA NDBC New Dungeness Buoy station 46088.

Significant wave height measurements are converted into sea state (Figure 4.9) using the WMO sea state categories from Table 1.3.

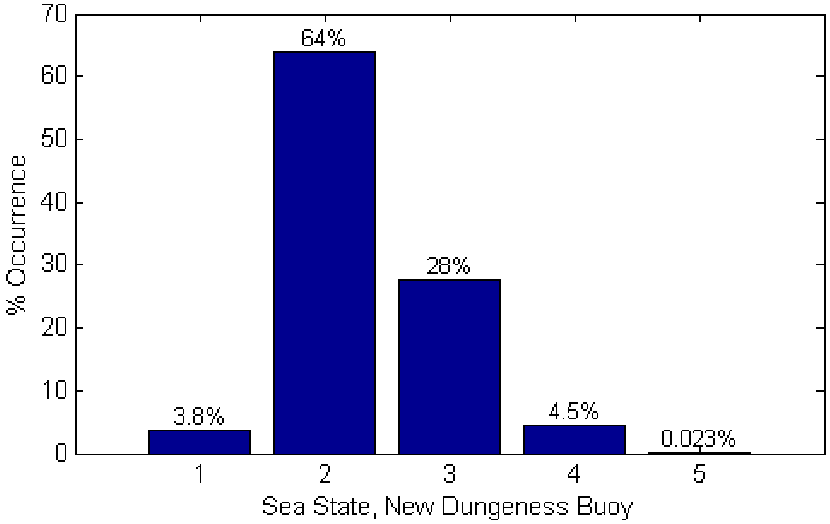

Figure 4.9 Distribution of sea state for the full year 2008. Calculated from significant wave height data from NOAA NDBC station 46088.

Following the findings of Baldacci et al., reliable detection is limited to sea state 1 or 2. As shown in Figure 4.9, these conditions occur 68% of the time.

4.4 IR Benefits Summary

Table 4.4 summarizes the benefit of infrared observation over visual observation in Admiralty Inlet, as quantified by the pass-fail criteria and meteorological data from 2008.

Table 4.4 Summary of the benefits of infrared observation over visual observation. Infrared shows a 28 percentage point increase over visual.

Parameters	Data Source	Visual		Infrared	
		Criteria	%	Criteria	%
Ambient Light	Field observations (Lime Kiln and Admiralty Inlet)	Between Civil Dawn & Dusk	56%	All hours	100%
Relative Humidity	Stull et al. (1964) and Wyatt et al. (1964).	All hours	100%	All hours	100%
Fog	Beier & Gemperleing (2004).	CAT I fog or below	99%	CAT I fog or below	99%
Sea State	Baldacci et al. (2005).	Sea State 2 or below	68%	Sea State 2 or below	68%
Composite		**All criteria satisfied**	**39%**	**All criteria satisfied**	**67%**

All four of the criteria must be satisfied for each hour to be considered as a pass for the combined percentage. The parameter with the greatest sensitivity is sea state (68%). If detection is possible in sea state 3, the combined results would change to 59% for visual and 95% for infrared (i.e. infrared detection could enable nearly continuous observation).

4.5 Additional Parameters

Additional parameters not considered in this evaluation include high sky temperature, sun glare, and precipitation. While not a consideration for this application, a high sky temperature can occur in tropical climates when there is cloud cover. Clouds can show an apparent temperature of up to 30 °C depending on the ambient air temperature (Jessup, 2004). If the sky temperature is greater than the sea temperature, the reflection of the sky may inhibit mammal detection by decreasing the target to sea surface temperature contrast. Additional field observations in a high sky temperature environment would be necessary to determine the degree to which marine mammal detection is affected.

Sun glare occurs when radiation from the sun is reflected off the surface of the sea and into the lens of the camera. The limited footage taken during high glare at Lime Kiln Park suggests that IR cameras are less affected than visible cameras. However, detection is difficult in both cases. Additional field measurements would be required to quantify the effects of sun glare.

Precipitation in the form of heavy showers and snow can also attenuate the IR signal. However, it is much easier for light to penetrate through a heavy shower than through a dense fog (Naboulsi, Sizen, & Fornel, 2004). This is because of the relatively lower density of rain droplets as compared to fog particles. Although it rains frequently at Admiralty Inlet, heavy precipitation or snow is rare and would not constitute a relevant change in effective monitoring time of an IR or visual camera.

Chapter 5 - IR Camera Selection Considerations

This chapter presents the most important factors to consider when choosing an infrared camera for marine mammal detection. Admittedly, it does not include all factors that will affect infrared imagery. For additional information, the reader is directed to listed references.

5.1 Resolution

As discussed in section 2.5, at least 2 pixels per target (PPT) are recommended for the detection of killer whale blows, and at least 9 pixels per target (PPT) are recommended for dorsal fin temperature measurement. These findings, along with target size and working distance, can be used to determine the appropriate infrared camera for a given deployment. Focal plane array resolution is restricted to commercially available sensors. Table 5.1 shows a summary of the typical FPA pixel resolutions currently available.

Table 5.1 Summary of commercially available infrared camera FPA pixel resolutions.

Horizontal Pixels Px_h	Vertical Pixels Px_v	Example Camera Models	Comments
320	240	FLIR A40M	Used for this study, 3 years old
640	480	ICI Prodigy 640 Pro FLIR A615 FLIR SC600 series Onca-LWIR-QWIP-640	Most current model infrared cameras
	512	FLIR SC6000 VarioTHERM (MWIR) FLIR Tau 640	High resolution and long range applications
1024	1024	FLIR SC8000	Highest FPA resolution currently available

Camera selection calculations can be greatly simplified by initially only considering the horizontal linear dimensions in the center of the desired field of view. Table 5.2 summarizes the variables required to determine the proper camera for a given deployment.

Table 5.2 Variables for infrared camera selection. Fixed variables are chosen depending on the deployment.

Site variables			
Variable	**Description**	**Units**	**Variable type**
T_h	Minimum target size.	meters (m)	Fixed
PPT_h	Horizontal Pixels per target.	pixels	Fixed
d_c	Distance to center of field of view.	meters (m)	Fixed
W_r	Required minimum width in the center of the field of view.	meters (m)	Fixed
W_c	Calculated width in the center of the field of view.	meters (m)	Calculated
Camera variables			
Variable	**Description**	**Units**	**Fixed/Dependent**
Px_h	Horizontal FPA resolution	pixels	Restricted to available equipment
Px_v	Vertical FPA resolution	pixels	Restricted to available equipment
α_c	Calculated angular field of view	Degrees	Calculated
α_a	Available angular field of view	Degrees	Restricted to available equipment

The first step is to select the fixed site variables (T_h, PPT_h, d_c, and W_r). For example, for marine mammal monitoring in Admiralty Inlet, the minimum target size is a killer whale dorsal fin. Although dorsal fins vary in size we will assume for this calculation that the horizontal width of a dorsal fin is approximately 0.5 meters. As shown in Figure 2.9, for a triangular target with a minimum of 9 pixels (PPT), the minimum number of horizontal pixels (PPT_h) is 5. The distance from Admiralty Head lighthouse to the proposed turbine site (d_c) is 1000 meters. It is desired to monitor at least 100 meters on either side of the proposed site. Since the turbines will be placed 50 meters apart, the minimum width in the vertical center of the field of view is 250 meters. Equation 5.1 is used to calculate the actual field of view for all commercially available pixels sizes. The resulting widths are show in Table 5.3.

$$W_c(m) = Px_h(pixels) * \left(\frac{T_h\ (m)}{PPT_h\ (pixels)}\right) \qquad 5.1$$

Table 5.3 Calculated width in the center of the field of view for Admiralty Inlet for a killer whale dorsal fin target.

Horizontal Pixels, Px_h (pixels)	Horizontal target size (fin), $T_h\ (m)$	Horizontal pixels per target (fin), PPT_h (pixels)	Calculated width in the vertical center of the field of view, W_c (m)
320	0.5	5	32
640	0.5	5	64
1024	0.5	5	102

The calculated width (W_c) is less than the specified minimum width (W_r) of 250 meters for all available pixel resolutions. In order to meet the specification a multiple camera solution is required. Three fixed cameras mounted side by side would provide a 306 meter width, but there would be no added benefit to vertical resolution. Another option is to use a foveal view system. In a foveal view system, one camera is used for detection (2 pixels per target, blow target), and a second camera is used to collect higher resolution images (9 pixels per target, dorsal fin target). Table 5.4 summaries the pros and cons of the two possible solutions. A foveal view system requires an automatic pan and tilt mechanism capable of positioning the second camera in the direction of detected targets. The benefits of a foveal view system were demonstrated by Podobna et al. (2010) who used multispectral imagers to position a digital video camera and an infrared camera in the EYE5 system (Section 1.4).

Table 5.4 Possible solutions for multiple camera systems.

Solution	Cameras required	Pros	Cons
Multiple fixed cameras	3	Low engineering effort	Higher camera cost
Foveal view system	2	Lower camera cost, Possible higher resolution images	High engineering effort

A foveal view system solution with two cameras (one low resolution for detection, and the second high resolution for identification and temperature measurement) will be adopted for this example. The low resolution will detect killer whale blows at 2 pixels per target and trigger a pan and tilt mechanism to position the high resolution camera. For whale blows the characteristic horizontal size is approximately 1 m. Repeating our calculations for the low resolution camera we arrive at the values shown in Table 5.5.

Table 5.5 Calculated width in the center of the field of view for Admiralty Inlet for a killer whale blow target.

Horizontal Pixels, Px_h (pixels)	Horizontal target size (blow), T_h (m)	Horizontal pixels per target (blow), PPT_h (pixels)	Calculated width in the vertical center of the field of view, W_c (m)
320	1	2	160
640	1	2	320
1024	1	2	512

For the low resolution camera, 640 horizontal pixels will allow for a maximum width in the center of the field of view of 320 meters which meets the specification (minimum of 250 meters). The next step is to calculate the required angular field of view (α_c) for both the low and high resolution camera optics. Equations 5.2 and 5.3 are derived from the camera geometry shown in Figure 5.1

where

s is the FPA sensor size,

f is the effective focal length of the camera and lens,

H is the height of the vertical field of view,

and the remaining variables are as described in Table 5.2.

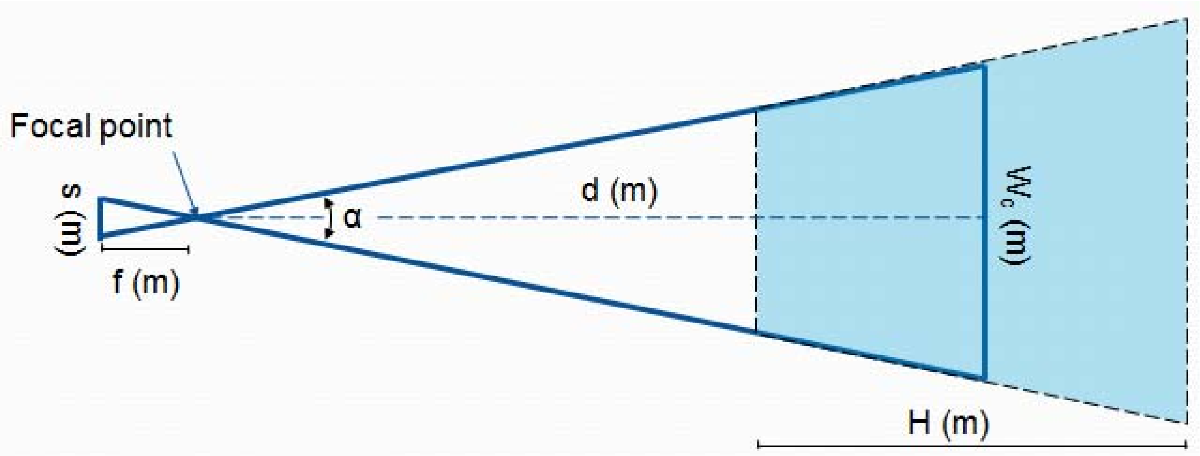

Figure 5.1 Camera geometry. The field of view is indicated in blue.

$$\alpha_c(degrees) = 2 * \tan^{-1}\frac{W\ (m)}{2 * d\ (m)} \tag{5.2}$$

$$f\ (m) = \frac{s}{2\tan(\alpha/2)} \tag{5.3}$$

Equation 5.2 is used to determine the required angular field of view (α_c). This is then compared to available lenses (α_a). For the low resolution camera, the maximum α_c is calculated using the minimum required width (W_r) of 250 meters, and the minimum is calculated using the calculated width (W_c) from Table 5.5. For the high resolution camera the calculated width (W_c) from Table 5.3 is used. In the interest of lowering camera cost, a camera with 640 horizontal pixels (as opposed to 1024) will be adopted for the high resolution camera. To determine the focal length from the calculated angular field of view, equation 5.3 is used. The sensor size (s) will vary depending on the specific camera selected. For this example a sensor size of 16 mm is assume which corresponds to a FPA pixel pitch of 25 μm and a horizontal pixel resolution of 640 pixels. Table 5.6 summarizes the required angular field of view (α_r) and the approximated focal length (f).

Table 5.6 Required angular field of view and estimated focal length.

Width (m)	Camera	Angular field of view (α_c, degrees)	Focal length for a 16 mm sensor (f, mm)
250	Low resolution, minimum width	14.3°	64 mm
320	Low resolution, maximum width	18.2°	50 mm
64	High resolution	3.7°	250 mm

For the low resolution camera, the calculated angular field of view ($14.3 \leq \alpha_c \leq 18.2$) falls within the range of commonly available lenses for LWIR cameras. For example, the FLIR SC600 (640 x 480 pixel resolution, 7.5-13 μm) offers an optional 15° FOV lens. Since the sensor size in the SC600 is 8 mm (pixel pitch of 17 μm) this corresponds to a 30 mm focal length. The Xenics Onca-LWIR-QWIP-640 (640 x 480 pixel resolution, 7.5-9 μm) offers an optional 18.2° lens (50 mm focal length).

The high resolution camera requires a narrow field of view (3.7°) which are only available on infrared cameras built for long range measurements, such as the FLIR SC6000 (640 x 512 pixel resolution, MWIR, 3-5 μm or LWIR, 8-9.2 μm). Table 5.7 lists the available lenses for the FLIR SC6000.

Table 5.7 Lenses available for FLIR SC6000

Spectral Band	Lens Focal Length	FOV
MWIR, 3 - 5 µm and LWIR, 8 - 9.2 µm	13 mm	56.4° x 90.3° FoV
MWIR, 3 - 5 µm and LWIR, 8 - 9.2 µm	25 mm	36.7 x 29.3° FoV
MWIR, 3 - 5 µm and LWIR, 8 - 9.2 µm	50 mm	18.3° x 14.7° FoV
MWIR, 3 - 5 µm only	100 mm	9.2° x 7.3° FoV
MWIR, 3 - 5 µm only	1000 mm	.92° x .73° FoV
MWIR, 3 - 5 µm only	**Dual Field of View: 50 and 250 mm**	**50 mm (18.3° x 14.7° FoV)**
		250 mm (3.7° x 2.9° FoV)
MWIR, 3 - 5 µm only	Triple Field of View: 60, 180, and 500 mm	60 mm (18.3° x 14.7° FoV
		180 mm (4.6° x 3.7° FoV)
		500 mm (1.5° x 2.4° FoV)

It can be seen that lenses for long range applications (focal length greater than 50mm) are only available for the MWIR sensor. Therefore, the high resolution camera for Admiralty Inlet would need to operate in the MWIR spectrum (3-5 µm). Since this study used a LWIR camera (7.5-14 µm), additional field observations are required to verify the efficacy of a MWIR camera for marine mammal detection. The “dual field of view” lens (show in bold below) could be used for verification in Admiralty Inlet. The calculations for selecting an appropriate infrared camera and lens are shown as a flow chart in Figure 5.2.

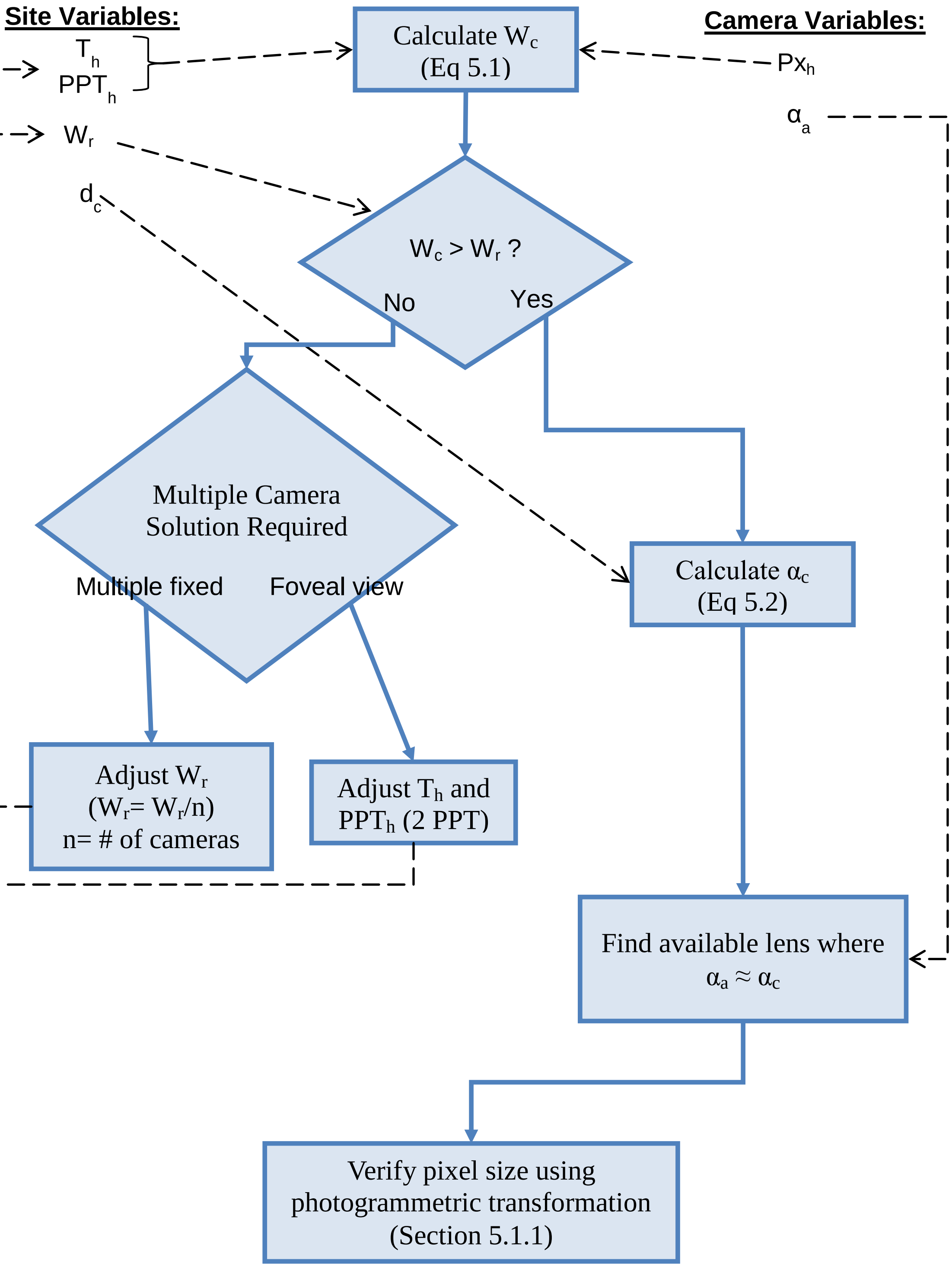

Figure 5.2 **Flow chart of infrared camera and lens selection calculations.**

5.1.1 Photogrammetric Transformation

For simplicity, the calculations shown above were all based on horizontal properties in the vertical center of the field of view. To determine if these approximations are adequate for both horizontal and vertical resolution a photogrammetric transformation is used to transform between 3-D world coordinates and 2-D image coordinates. For this study, the methods of Holland et al. (1997) are used. For verifying camera selection, a direct linear transformation (DLT) is used to approximate the pixel size assuming no distortion. This is accomplished using equation 2 from the listed reference (Holland, Holman, Lippmann, Stanley, & Plant, 1997). Figure 5.3 shows the estimated field of view for the proposed low resolution (FLIR SC600 with 15° FOV lens) and high resolution (FLIR SC6000 with 3.7° FOV lens) cameras.

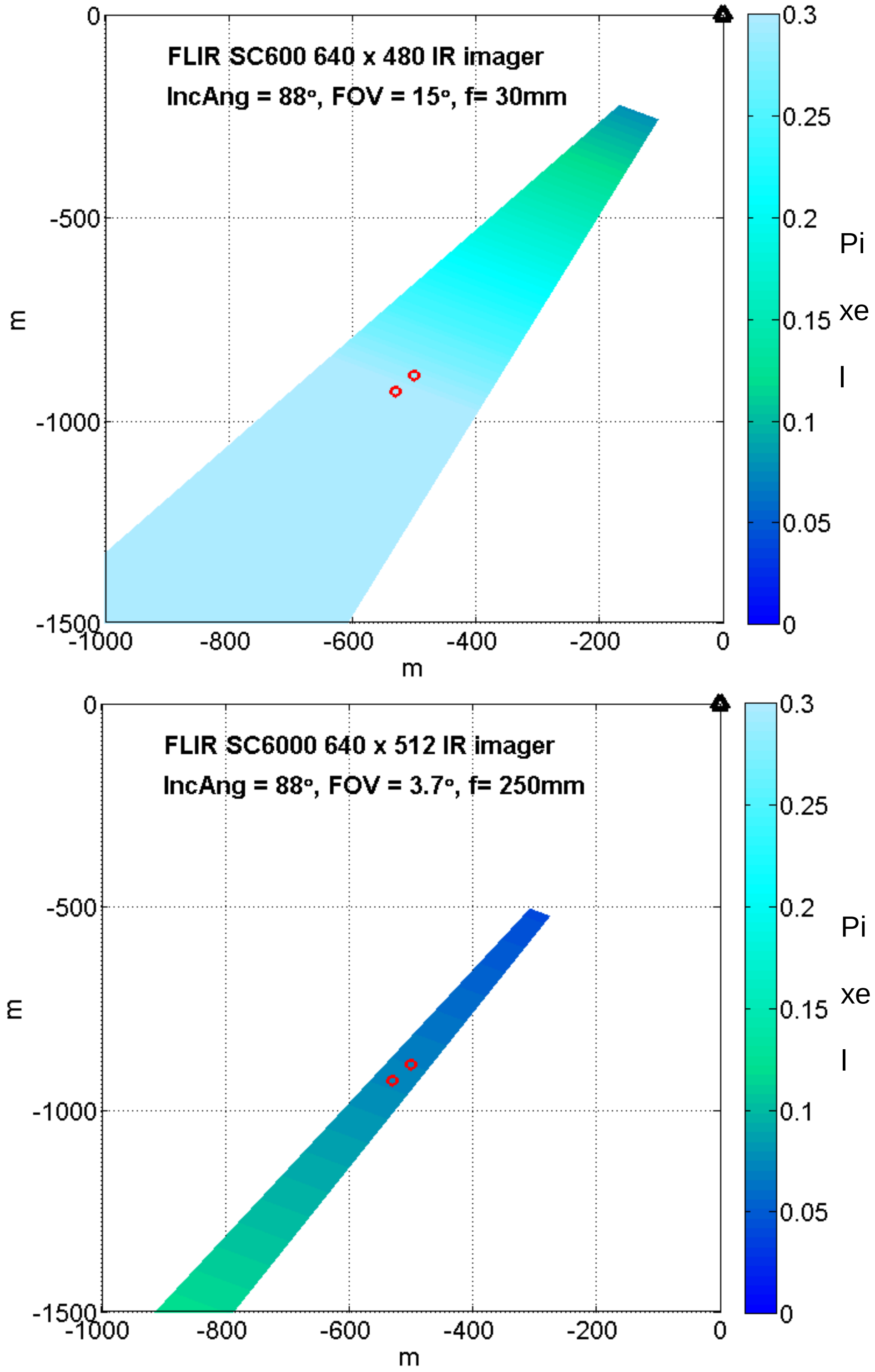

Figure 5.3 Estimated field of view at Admiralty Inlet for the proposed low resolution camera (FLIR SC600 with optional 15° FOV, f= 30 mm lens) and high resolution camera (FLIR SC6000 with optional 3.7° FOV, 250 mm lens). Camera location indicated by the black triangle at the origin. The proposed tidal turbine sites are shown as red circles. X-axis is positioned east (negative) to west (positive) and Y-axis is positioned north (positive) to south (negative).

In order to calculate accurate pixel sizes for the entire field of view it’s necessary to take into account pixel distortion. Pixel distortion for an individual camera and lens combination can be measured using the methods of Holland et al. (1997). Holland et al. used a uniform grid of white circles on a black background for measuring the pixel distortion of visual cameras. For infrared cameras, a similar approach is used, but instead of a grid of color contrast, it’s necessary to create a grid of apparent temperature contrast. This can be accomplished by combining materials of high reflectivity, such as aluminum foil, with materials of high emissivity, such as poster board. For pixel distortion measurement of the FLIR A40M used in this study, a uniform grid of aluminum foil was attached to white poster board. Since the aluminum foil is highly reflective to infrared radiation and the poster board is not, the apparent temperature contrast can be clearly seen by an infrared imager. The radial distortion can then be measured. Once the radial distortion is measured it is converted to distortion coefficients as described by Holland et al. The transformation requires complex calculations and instead of repeating the equations here, the reader is directed to the listed reference (Holland, Holman, Lippmann, Stanley, & Plant, 1997).

5.2 Non-uniformity Correction

As discussed in sections 1.3 and 2.4, uncooled microbolometer based infrared cameras require frequent non-uniformity correction (NUC) due to sensor and lens drift with ambient temperature. Many modern cameras (such as the FLIR A40M used in this study) include an internal blackbody and automatic NUC function.

Since these blackbodies are located behind the lens of the camera they correct for non-uniformities of the sensor only. The camera NUC function for this model includes a look-up table that provides the expected transmission of the lens at a range of ambient temperatures. Although these functions are useful for removing noise from the collected image, they cannot account for changes of the external optical equipment such as dirt on the lens, or lens transmission changes over time (Jacobs, 2006). Cameras calibrated with internal blackbodies alone provide accurate temperature contrasts, but not absolute temperatures. If accurate absolute temperature measurements are required, frequent calibration must be completed using an external blackbody at a known temperature, see Jacobs (2006).

5.3 Absolute Temperature Measurement

Marine mammals are detected in this study by temperature contrast. As discussed in Section 2.6.2, this temperature contrast is greatly influenced by sea surface emissivity at high incidence angles. As discussed in section 2.6, to correct for emissivity and obtain an accurate measurement of absolute temperature, both the sea and sky temperature must be known. An accurate sky temperature measurement can be obtained by using an infrared radiometer (or second infrared camera) facing the sky at a zenith angle equal to the incidence angle of the camera viewing the sea surface. Sky temperature measurements can then be used to calculate the absolute surface temperature from the apparent surface temperature using equation 1.14.

Chapter 6 - Conclusions

A land-based infrared camera (FLIR Thermovision A40M, 7.5-14µm, 37°HFOV, 320x240 pixels) was used to detect Southern Resident killer whales from Lime Kiln park in Washington State. The primary purpose of this study is to evaluate the efficacy of infrared imagery for monitoring marine mammals at a proposed tidal energy pilot project in northern Admiralty Inlet, Puget Sound. Results from a field study at a nearby site demonstrate the successful detection of killer whales (body, dorsal fin, and blow) during both day and night at ranges from 43 to 162 meters. Whales at distances greater than 100 meters were identified primarily by their blows and suggest a minimum of 2 pixels per target for detection.

The apparent dorsal fin to sea temperature contrast shows dependence on both the number of pixels per target and incidence angle. For a killer whale dorsal fin, at least 9 pixels per target are necessary to minimize the effects of pixel averaging on maximum observed temperature contrast. The apparent fin to sea temperature contrast increases with incidence angle. This increase is shown to be related to the reflection of sky radiation due to increased surface reflectivity at near-grazing angles. Observations are in agreement for predicted increase of fin to sea temperature contrast with incidence angle.

Compared to visual cameras, infrared cameras offer a more limited range of available pixel resolutions and camera optics (zoom, lenses). Infrared cameras also require frequent non-uniformity correction. As a result, additional care must be taken in designing an infrared monitoring solution. The benefits of infrared imagery include the addition of night-time detection which increases the hours of possible detection.

For the case study of Admiralty Inlet, observation time increases by 75% (28% percentage point increase) for infrared-based systems versus visual detection.

The implementation of automated detection is simplified by detecting temperature gradients instead of motion. A simple algorithm is developed that reduced frames requiring review by 94% and identifies 85% of surfacing whales. Further refinement is required to reduce the number of missed detections and false-positives.

For Admiralty Inlet, a land-based infrared monitoring system would need to include at least two cameras. The first camera (FLIR SC600 with a 15° FOV lens or equivalent) would provide a horizontal field of view of 320 meters at a distance of 1 km and 2 pixels per target for a 1 m x 1 m target. A second camera (FLIR SC6000 with 3.7° FOV lens or equivalent) would provide high resolution images at 9 pixels per target at a distance of 1 km. Engineering effort would be required to implement these cameras in a foveal view system. The first camera, mounted in a fixed position, would be used for detection. As soon as a target is identified the second camera could be rotated to collect high resolution images.

6.1 Future Study

There are relatively few studies that are directly applicable to infrared detection of marine mammals, leaving ample room for future study on this topic. A long-term deployment of an infrared and visible camera system at a site with a known marine mammal population (such as Lime Kiln Park) would allow for footage of marine mammals to be recorded in a variety of environmental conditions. A mobile weather station should be co-located with the camera system to monitor air and water temperature, relative humidity, wind speed, wind direction, and visibility. In addition, sky temperature should be monitored using an infrared radiometer. This would allow for further clarification of the limitations associated with detection at high sea states, the detection range for marine mammal targets during fog, and the negative effects of precipitation. Detection during periods of sun glare could be analyzed and criteria established for minimizing the effects. A method that provides frequent, automated non-uniformity corrections of the IR camera should be developed to minimize signal and lens drift during extended recording periods.

Development and implementation of a foveal view (nested FOV) camera system would enable the recording of high resolution images in the specific area of detection. This would, however, more than double the cost of the monitoring system in terms of equipment and engineering integration time.

GLOSSARY

Term	Abbreviation (if used)	Definition
Absorption		Attenuation of electromagnetic radiation due to a portion of the photon energy being converted to another form such as vibrational or rotational energy of the atoms or molecules in its path.
Absorptivity	α	The fraction of electromagnetic energy (irradiance) absorbed by a surface or medium.
Apparent Temperature		The temperature of a blackbody that produce the same spectral radiance as an observed real body
Astronomical Dawn		The time in early morning when the sun is 18° below the horizon. The start of morning astronomical twilight
Astronomical Dusk		The time in late evening when the sun is 18° below the horizon. The end of evening astronomical twilight
Astronomical Twilight		The period of time when the sun is between 12°and 18° below the horizon. There are two periods of astronomical twilight each day, one in early morning and one in late evening.
Atmospheric Mass	M_a	A measure of the amount of atmosphere passed through in a given light of sight. $M_a=1$ is equal to the path length through the atmosphere at the zenith ($\theta_z=0$).
Attenuation		The degradation of electromagnetic radiation intensity as it propagates through a medium.
Blackbody	bb	An ideal body that absorbs all incident energy and reflects none at all αvelengths and at all angles of incidence. A blackbody is also a perfect emitter. $\varepsilon_{bb} = \alpha_{bb} = 1$
Category 5	CAT5	A twisted pair high signal integrity cable type often referred to as CAT5 or simply an Ethernet cable.
Charge-coupled Device	CCD	A silicon-based photoelectric detector which contains thousands of light-sensitive cells that convert light (visible and NIR) to voltage. Used in most digital cameras.

Civil Dawn		The time in early morning when the sun is 6° below the horizon. The start of morning civil twilight
Civil Dusk		The time in late evening when the sun is 6° below the horizon. The end of evening civil twilight
Civil Twilight		The period of time when the sun is between 0°and 6° below the horizon. There are two periods of civil twilight each day; one in early morning, between dawn and sunrise; and one in late evening, between sunset and dusk.
Electromagnetic Radiation		Energy that is transmitted as a stream of photos (massless particles) moving at the speed of light (*c*). (a.k.a. light)
Emissivity	ε	The ratio of the total power emitted (emmitance) by a surface or body to the total power emitted from a blackbody at the same temperature.
Emmitance	M	The flux density emitted from a surface or body (a.k.a. exitance).
Field of View	FOV	The total area "seen" by a camera. May be expressed in units of distance (m) or degrees (angular FOV).
Flux	Φ	Energy per unit time. (watts)
Flux Density	I or M	Flux per unit area. (W/m^2)
Focal Length	f	The distance from a lens to the point where it is focused. May be expressed in units of distance (mm) or degress.
Focal Plane Array	FPA	A 2D array of light sensing pixels. Commonly used to refer to the sensors in infrared cameras.
Graybody		A body or surface with an emissivity that is independent of wavelength ($\varepsilon(\lambda)= \varepsilon$)
Horizontal Field of View	HFOV	The horizontal component of the field of view (FOV). May be expressed in units of distance (m) or degrees.
Incidence Angle	θ	The angle between a downward pointing vector (e.g. normal to the sea surface) and a given line of sight.
Infrared	IR	Electromagnetic radiation with wavelengths between 1 and 100 µm.
International Civil Aviation Organization	ICAO	The United Nations agency concerned with civil aviation. For this study, the ICAO categorization of fog was used.
Irradiance	I	Flux density incident on a surface or body.

Long Wave Infrared	LWIR	Electromagnetic radiation with wavelengths between 8 and 14 µm.
Medium Wave Infrared	MWIR	Electromagnetic radiation with wavelengths between 3 and 5 µm.
Microbolometer		A small version of a bolometer which is a device for measuring the energy of electromagnetic radiation typically in the LWIR range.
MODTRAN		An atmospheric radiative transfer model developed by Spectral Sciences inc. and the US Air Force Research Laboratory. Serves as the standard atmospheric band model for the remote sensing community. Abbreviation of MODerate Resolution Atmospheric Radiance and TRANsmittance Model.
National Climatic Data Center	NCDC	The division of NOAA that maintains the world's largest active archive of weather data. For this study, the climate data from the Whidbey Island NAS was obtained from NCDC.
National Data Buoy Center	NDBC	The division of NOAA that designs, develops, operates, and maintains a network of data collecting buoys and coastal stations. For this study, climate data from the New Dungeness buoy was used.
National Oceanic and Atmospheric Administration	NOAA	An agency in the Department of Commerce that maps the oceans and conserves their living resources.
Nautical Dawn		The time in early morning when the sun is 12° below the horizon. The start of morning nautical twilight
Nautical Dusk		The time in late evening when the sun is 12° below the horizon. The end of evening nautical twilight
Nautical Twilight		The period of time when the sun is between 6°and 12° below the horizon. There are two periods of nautical twilight each day; one in early morning, and one in late evening.
Naval Air Station	NAS	An air station for the US Navy, frequently abbreviated NAS.
Near Infrared	NIR	Electromagnetic radiation with wavelengths between visible (0.77 um) and infrared (1 µm).
Noise Equivalent Temperature Difference	NETD	A measurement of the internal noise of an infrared camera given in units of temperature.

Non-uniformity Correction	NUC	The Correction of an infrared camera performed by pointed the camera at a blackbody of known uniform temperature and adjusting for any non-uniformities.
Pass		A collection of continuous whale surfacing events with no gaps (where no whales can be seen in the footage) longer than 1 minute.
Pixels per Target	PPT	The number of pixels that make up a given target.
Power Over Ethernet	POE	A system of providing electrical power as well as data over a single CAT5 cable.
Reflectivity	ρ	The fraction of electromagnetic energy (irradiance) reflected by a surface.
Relative Humidity	RH	The ratio of the amount of water in the air at a given temperature to the maximum amount it could hold at that temperature.
Runway Visual Range	RVR	The distance where visible image contrast is degraded by 98%. Used to measure visibility at airports. (a.k.a. visibility)
Scattering		When the path of electromagnetic radiation is altered by particles in its path.
Short Wave Infrared	SWIR	Electromagnetic radiation with wavelengths between 1 and 3 µm.
Significant Wave Height	SWH	An average measurement of the largest 33% of waves.
Surfacing Event		A collection of continuous frames showing a single whale above the sea surface. If a single whale surfaces multiple times in the FOV this counts as multiple surfacing events.
Target Size	TGT	The size of a desired target.
Temperature Contrast		The difference between a target and its background. For this study used primarily to describe the difference between a detected dorsal fin and the surrounding sea surface.
Transmissivity	τ	The fraction of electromagnetic radiation transmitted through a medium.
Twilight		The period before sunrise and after sunset where visible light from the sun is reflected from the upper atmosphere. Can be separated into civil, nautical, and astronomical twilight.

Very Long Wave Infrared	VLWIR	Electromagnetic radiation with wavelengths between 14 and 100 µm.
Visibility		The distance where visible image contrast is degraded by 98%. (a.k.a. runway visible range, RVR)
World Meteorological Organization	WMO	United Nations agency concerned with the international collection of meteorological data. For this study the WMO sea state categorizes were used.
Zenith Angle	θ_z	An angle between two lines in a vertical plane where one of the lines is directed towards zenith (directly upward).

BIBLIOGRAPHY

American Society for Testing and Materials. (1992). *Reference solar spectral irradiance: Air mass 1.5*. Retrieved February 9, 2011, from Renewable resource data directory: http://rredc.nrel.gov/solar/spectra/am1.5/

Baldacci, A., Carron, M., & Portunato, N. (2005). Infrared detection of marine mammals. *Technical report SR-443*. NATO Undersea Research Centre.

Beier, K., & Gemperlein, H. (2004). Simulation of infrared detection range at fog conditions for enhanced vision systems in civil aviation. *Aerospace Science and Technology, 8*, pp. 63-71.

Cuyler, L. C., Wiulsrod, R., & Oritsland, N. A. (1992, April). Thermal infrared radiation from free living whales. *Marine Mammal Science, 8*(2), 120-134.

Dhar, V., & Khan, Z. (2008, May 10). Comparison of modeled atmosphere-dependent range performance of long-wave and mid-wave IR imagers. *Infrared Physics & Technology, 51*, pp. 520-527.

Filipiak, M. (2008). Refractive indices (500-3500 cm-1) and emissivity (600-3350 cm-1) of pure water and seawater. *[Dataset]*.

Greene, C. R., & Chase, S. C. (1987). *Infrared detection of whale spouts.* Shell Western E&P Inc. Santa Barbara: Greeneridge Sciences, Inc.

Holland, K. T., Holman, R. A., Lippmann, T. C., Stanley, J., & Plant, N. (1997, January). Practical use of video imagery in nearshore oceanographic field studies. *IEEE Journal of Oceanic Engineering, 22*(1), 81-92.

Jacobs, A. P. (2006). *Thermal infrared characterization of ground targets and backgrounds* (Second ed.). Bellingham, Washington: SPIE.

Jessup, A. (2004). *CIRIMS 2 onboard the R/V Thomas G. Thompson, Japan to Seattle 6/21/06 to 7/6/04, Version 1.0*. Retrieved February 9, 2011, from CIRIMS data archive: http://cirims.apl.washington.edu/DataFiles/CIRIMS04_Japan_Seattle_v1.0.txt

Jessup, A. T., & Branch, R. (2008). Integrated ocean skin and bulk temperature measurements using the calibrated infrared in situ measurement system (CIRIMS) and through-hull ports. *Journal of Atmospheric and Oceanic Technology, 25*, 579-597.

Jessup, A., Chickadel, C., & Stafford, K. (2009). *Evaluation of infrared imagery for marine mammal detection from ship-based platforms.* A proposal to ONR BAA Number 09-105, Seattle.

Kasting, N. W., Adderley, S. A., Safford, T., & Hewlett, K. G. (1989). Thermoregulation in beluga (Delphinapterus leucas) and killer (Orcinus orca) whales. *Physiological Zoology, 62*(3), 687-701.

Kruse, P. W., McGlauchlin, L. D., & McQuistand, R. B. (1962). *Elements of infrared technology: generation, transmission, and detection.* New York: John Wiley & Sons, Inc.

Maghrabi, A., & Clay, R. (2010). Precipitable water vapour estimation on the basis of sky temperatures measured by a single-pixel IR detector and screen temperatures under clear skies. *Meteorological Applications, 17*, 279-286.

Maldague, X. (2007). *Multipolar infrared vision theory*. Retrieved February 16, 2011, from MIVIM: http://mivim.gel.ulaval.ca/dynamique/index.php?idM=57&Lang=

Naboulsi, M. A., Sizen, H., & Fornel, F. d. (2004, February). Fog attenuation prediction for optical and infrared waves. *Optical Engineering, 43*(2), pp. 319-329.

National Instruments. (2001). *Calculating camera sensor resolution*. Retrieved February 16, 2011, from KnowledgeBase: http://digital.ni.com/public.nsf/allkb/29D716D6F4F1FBC386256AE700727AF6

National Marine Fisheries Service. (2008). *Recovery Plan for Southern Resident Killer Whales (Orcinus orca).* Seattle, Washington: National Marine Fisheries Service, Northwest Region.

NNMREC. (2010). *Fundamentals of tidal energy*. Retrieved February 23, 2011, from Northwest National Marine Renewable Energy Center (NNMREC), University of Washington Branch: http://depts.washington.edu/nnmrec/overview.html

Perryman, W. L., Donahue, M. A., Laake, J. L., & Martin, T. E. (1999). Diel variation in migration rates of eastern Pacific gray whales measured with thermal imaging sensors. *Marine Mammal Science, 15*(2), 426-445.

Podobna, Y., Sofianos, J., Schoonmaker, J., Medeiros, D., & Boucher, C. (2010). Airborne multispectral detecting system for marine mammals survey. *Ocean Sensing and Monitoring II. 7678.* Orlando, FL: SPIE.

Schoonmaker, J., Dirbas, J., Podobna, Y., Wells, T., Boucher, C., & Oakley, D. (2008). Multispectral observations of marine mammals. *Electro-optical and infrared systems: Technology and application V. 7113.* Bellingham, WA: SPIE.

SeaWorld Parks & Entertainment. (2011). *Killer whale physical characteristics*. Retrieved February 16, 2011, from SeaWorld/Busch Gardens animals: http://www.seaworld.org/animal-info/info-books/killer-whale/physical-characteristics.htm

Snohomish County PUD. (2009). *Tidal: OpenHydro*. Retrieved February 23, 2011, from Power Supply: http://www.snopud.com/PowerSupply/tidal/tidalbg/tidalopenhydro.ashx?p=1511

Stull, V. R., Wyatt, P. J., & Plass, G. N. (1964, February). The infrared transmittance of carbon dioxide. *Applied Optics, 3*(2), pp. 243-254.

Tans, P. (2010). *NOAA/ESRL*. Retrieved January 30, 2011, from Trends in atmospheric carbon dioxide: http://www.esrl.noaa.gov/gmd/ccgg/trends/

The Whale Museum. (2006). *Days/months the Orcas have been detected in Puget Sound*. Retrieved February 12, 2011, from http://www.whale-museum.org/education/library/whalewatch/pugetsound.html

Trucco, E., & Plakas, K. (2006, April). Video tracking: A concise survey. *IEEE Journal of Oceanic Engineering, 31*(2), 520-529.

U.S. Naval Observatory. (2011). *Astronomical applications*. Retrieved February 25, 2011, from Naval oceanography portal: http://www.usno.navy.mil/USNO/astronomical-applications

US Energy Information Administration. (2010, January 20). *Washignton state energy profiles*. Retrieved February 21, 2011, from State & U.S. historical data: http://www.eia.gov/cfapps/state/state_energy_profiles.cfm?sid=WA#Datum

Wayne, F. D. (1991, January). An economical formula for calculating atmospheric infrared transmissivities. *J. Loss Prev. Process Ind., 4*, pp. 86-92.

Wyatt, P. J., Stull, V. R., & Plass, G. N. (1964, February). The infrared transmittance of water vapor. *Applied Optics, 3*(2), pp. 229-241.

Zappa, C. J. (1994). *Infrared field measurements of sea surface temperature: Analysis of wake signatures and comparison of skin layer models.* Seattle: Applied Physics Laboratory, University of Washington.

Zissis, G. J., Accetta, J. S., & Shumaker, D. L. (1993). *The infrared and electro-optical systems hand book* (Vols. Volume-1: Sources of Radiation). Bellingham, Washington: SPIE Optical Engineering Press.